Computation and Analysis of EGR Mixing in Internal Combustion Engine Manifolds

by

Alexander Sakowitz

February 2013
Technical reports from
Royal Institute of Technology
Department of Mechanics
SE-100 44 Stockholm, Sweden

Akademisk avhandling som med tillstånd av Kungliga Tekniska Högskolan i Stockholm framlägges till offentlig granskning för avläggande av teknologie doktorsexamen fredag den 22 februari 2013 kl 10.15 i sal F3, Lindstedtsvägen 26, Kungliga Tekniska Högskolan, Stockholm.

TRITA-MEK Technical report 2013:02
ISSN 0348-467X
ISRN KTH/MEK/TR–13/02–SE
ISBN 978-91-7501-639-9

©Alexander Sakowitz 2013
Universitetsservice US–AB, Stockholm 2013

Computation and Analysis of EGR Mixing in Internal Combustion Engine Manifolds

Alexander Sakowitz, 2013

CCGEx & Linné Flow Centre, KTH Mechanics, Royal Institute of Technology
SE-100 44 Stockholm, Sweden

Abstract

This thesis deals with turbulent mixing processes occurring in internal combustion engines, when applying exhaust gas recirculation (EGR). EGR is a very efficient way to reduce emissions of nitrogen oxides (NO_x) in internal combustion engines. Exhaust gases are recirculated and mixed with the fresh intake air, reducing the oxygen concentration of the combustion gas and thus the peak combustion temperatures. This temperature decrease results in a reduction of NO_x emissions. When applying EGR, one is often faced with non-uniform distribution of exhaust among and inside the cylinders, deteriorating the emission performance. The mixing of exhaust gases and air is governed by the flow in the engine intake manifold, which is characterized by unsteadiness due to turbulence and engine pulsations. Moreover, the density cannot be assumed to be constant due to the presence of large temperature variations.

Different flow cases having these characteristics are computed by compressible Large Eddy Simulations (LES). First, the stationary flows in two T-junction type geometries are investigated. The method is validated by comparison with experimental data and the accuracy of the simulations is confirmed by grid sensitivity studies. The flow structures and the unsteady flow modes are described for a range of mass flow ratios between the main and the branch inlet. A comparison to RANS computations showed qualitatively different flow fields.

Thereafter, pulsating inflow conditions are prescribed on the branch inlet in order to mimic the large pulsations occurring in the EGR loop. The flow modes are investigated using Dynamical Mode Decomposition (DMD).

After having established the simulation tool, the flow in a six-cylinder engine is simulated. The flow is studied by Proper Orthogonal Decomposition (POD) and DMD. The mixing quality is studied in terms of cylinder-to-cylinder non-uniformity and temporal and spatial variances. It was found that cycle-averaging of the concentration may give misleading results. A sensitivity study with respect to changes in the boundary conditions showed that the EGR pulsations, have large influence on the results. This could also be shown by POD of the concentration field showing the significance of the pulses for the maldistribution of exhaust gases.

Finally, the flow in an intake manifold of a four-cylinder engine is investigated in terms of EGR distribution. For this geometry, pipe bends upstream of the EGR inlet were found to be responsible for the maldistribution.

Descriptors: Turbulent Mixing, Large Eddy Simulation, URANS, Internal Combustion Engines, Intake Manifolds, T-junction, Exhaust Gas Recirculation

Preface

This thesis consists of two parts. The first part gives an introduction into the field of emission formation in internal combustion engines, the computation of turbulent flows and mixing processes and a summary of selected results. The second part consists of 4 papers discussing the results more detailed. The papers have been adjusted to the thesis format, while keeping the content in the original form.

February 2013, Stockholm
Alexander Sakowitz

Contents

Abstract iii

Preface iv

Part I. Overview and Summary

Chapter 1. Introduction 1

Chapter 2. Background 4
2.1. T-junctions 4
2.2. Pulsating flow in pipes 5
2.3. EGR mixing 6
2.4. Contribution of this thesis 6

Chapter 3. Emissions of Internal Combustion engines 8
3.1. IC engine cycles 8
3.2. Combustion and emissions 9
3.3. Reduction of emissions 11

Chapter 4. Turbulence and turbulent mixing 15
4.1. The energy cascade and Kolmogorov's hypotheses 15
4.2. Turbulent mixing 16

Chapter 5. Computation of turbulent mixing 19
5.1. Governing equations 19
5.2. Modeling of turbulence and turbulent mixing 21
5.3. Boundary conditions 25
5.4. Numerics 25
5.5. Evaluation of mixing quality 29
5.6. Flow Decomposition methods 31

Chapter 6. Selected results and discussions 35
6.1. Flow and mixing in T-junctions 35
6.2. EGR mixing in the Scania manifold 44
6.3. Comparison to a symmetric Volvo inlet manifold 50

Chapter 7. Conclusions and future research perspectives 53

Chapter 8. Papers and Authors' Contributions 56
Paper 1 56
Paper 2 56
Paper 3 57
Paper 4 57

Acknowledgements 59

References 60

Part II. Papers

Paper 1. Turbulent flow mechanisms in mixing T-junctions by Large Eddy Simulations 67

Paper 2. Effects of velocity ratio and inflow pulsations on the flow in a T-junction by Large Eddy Simulation 93

Paper 3. Modeling of EGR Mixing in an engine intake manifold using LES 119

Paper 4. Flow decomposition methods applied to the flow in an IC engine manifold 137

Part I

Overview and Summary

CHAPTER 1

Introduction

This thesis deals with the mixture formation of exhaust gases and air in internal combustion engines (ICE). Modern combustion engines - primarily Diesel engines, but recently also gasoline engines - use Exhaust Gas Recirculation (EGR) in order to decrease the peak combustion temperatures and thereby control the NO_x emissions of the engine. The mixing between exhaust gases and intake air affects the emissions and the performance of the engine. However, turbulent mixing processes are of high importance also in other applications. Some examples are the mixing of air and fuel in gas turbines or in the cylinders of ICE, mixing of hot and cold water in power plant applications, or chemical applications, where the mixing quality of two reacting substances determines the reaction rate. The understanding of turbulent mixing processes and of the underlying flow mechanisms is therefore interesting also in a broad sense.

EGR is a concept of reducing NO_x emissions of ICE. The working principle is illustrated in Fig. 1.1. A portion of the exhaust gases is recirculated and mixed with the intake air. Non-uniformity of this mixture has a deteriorating effect on the engine performance and engine emissions, as shown experimentally by Maiboom *et al.* (2009). NO_x emissions are the main cause for photochemical smog and are problematic for both Diesel and Otto engines. Car and truck manufacturers are therefore facing strong regulations on the limits of NO_x emissions. Thus, the understanding, prediction and optimization of the mixing process between EGR and air is of high interest for industrial applications. Other issues with EGR, not addressed in this thesis, are the condensation of water contained in the exhaust gases and the deposition of soot particles inside the manifolds.

The objective of this thesis is to examine mixing processes in engine-like conditions and to assess different modeling approaches, namely Reynolds averaged Navier-Stokes (RANS) and Large Eddy Simulation (LES). Furthermore the physics governing the mixing process are analyzed based on these computations. Apart from the modeling approach, the Boundary Conditions (BCs) are crucial when performing numerical simulations because the real BCs as they occur in an engine are difficult to determine and have to be estimated. The effect of variations in the BCs are analyzed in order to identify the most important BCs and to assess the uncertainty of the predictions due to the uncertainty in the BCs.

Due to downsizing and other optimization strategies, engine manifolds are often very complex geometries. Additionally, one has to deal with large flow pulsations,

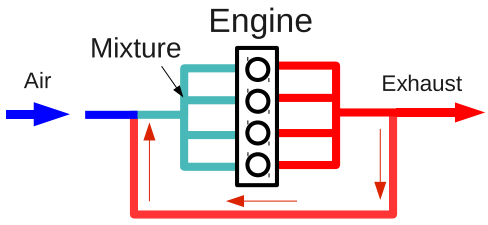

FIGURE 1.1. Schematic of Exhaust gas recirculation (for short-route EGR without EGR cooler and turbocharger)

high Reynolds numbers and temperature gradients. The results of well-resolved flow computations are therefore not always straight-forward to interpret. Therefore, different post-processing methodologies such as Proper Orthogonal Decomposition (POD) and Dynamic Mode Decomposition (DMD) are investigated for the use in the engine context.

The approach to the engineering problem is to first investigate simpler geometries, in which similar mixing processes occur. Such a geometry is a T-junction. The turbulent flow and the mixing process in two different T-junction geometries with a velocity ratio of 1 between the branches are studied in Paper 1. The grid dependence of the solution is assessed and the results are compared to experimental data. Furthermore, the secondary flow structures and the flow modes are analyzed.

Paper 2 analyzes the flow structures and the flow modes in a T-junction with varying velocity ratios and with pulsating inflow conditions at the branch inlet, mimicking the pulsations originating from the exhaust pulses. The impact of the flow phenomena on the concentration distribution is shown. DMD is performed in order to extract vortex shedding phenomena from the highly pulsating flow.

In Paper 3 the LES method is applied to the inlet manifold of a realistic six cylinder Diesel engine, which was provided by Scania. The boundary conditions for this case were taken from one-dimensional computations, partly from experiments performed in cooperation with another student inside the Competence Center for Gas Exchange (CCGEx). Explanations for the observed non-uniformity are given and the sensitivity to changes of the boundary conditions is assessed. Paper 4 complements these findings by POD and DMD results, giving an enhanced understanding of the flow field.

The thesis will start by giving the background of the recent research related to this work in chapter 2. It is followed by an introduction to emission formation and the most common ways of emission reduction (Chapter 3). Thereafter, Chapter 4 treats some theoretical aspects of turbulence and passive scalar mixing. Chapter 5 will introduce

the concepts used for the computation and post-processing analyses of turbulent flows and mixing processes. A summary and a discussion of the most important results is given in Chapter 6. Finally, Chapter 7 will conclude the thesis by summarizing the most important conclusions and giving a perspective on possible future research directions.

CHAPTER 2

Background

Flows in engine manifolds exhibit many different fluid dynamical phenomena. Common for engine geometries is the occurrence of pipe bends and junctions. Furthermore, the flows are pulsating due to moving valves. This section is intended to give a short review of flow and mixing processes related to these types of environments.

2.1. T-junctions

As a test case for the numerical method and for the investigation of flow mechanisms, simplified geometries are more suited than complex engine geometries. T-junctions of circular pipes or square ducts are such simplified geometries, in which similar flow phenomena as in engine geometries can be expected. The flow in T-junctions including mixing of passive scalars under stationary flow conditions has been investigated in several computational and experimental studies.

On the experimental side, Brücker (1997) applied Particle Image Velocimetry (PIV) in order to obtain the mean and instantaneous flow in a circular T-junction at comparably small Reynolds numbers ($< 3,000$). Some of the vortical structures including counter-rotating vortices directly downstream of the junction were described. A passive scalar quantity was not measured in these experiments. Further experiments were performed in a circular T-junction by Andersson *et al.* (2006) using Laser Doppler Velocimetry (LDV) and thermocouples providing a valuable data base for validation of computational results, including higher-order statistics for the velocity and temperature at Reynolds numbers up to 100,000. Inflow conditions were carefully documented. Another experiment using PIV on a T-junction with rectangular cross-sections is reported by Hirota *et al.* (2006). Additionally to the mean and Root Mean Square (RMS) of velocity and temperature, the turbulent scalar fluxes could be obtained by simultaneous measurement of velocity and temperature. This data is of particular use for the assessment of scalar flux models. Experiments and computations on a T-junction with a diameter ratio between the main and the branch pipe of 3 were performed by Kamide *et al.* (2009). Due to the large diameter ratio, this configuration resembles more a jet-in-crossflow configuration than a classical T-junction. Dominant temperature fluctuations were found at a normalized frequency of 0.2 based on the branch pipe diameter and the bulk velocity in the main pipe. These fluctuations were explained by vortex shedding phenomena similar to von-Karman vortices downstream of a cylinder.

On the computational side, a larger number of studies have been performed, mostly motivated by thermal fatigue due to temperature fluctuations in power plant applications. Steady-state RANS has been applied by Kok & van der Wal (1996) and Walker *et al.* (2010). In these studies it was concluded that *ad-hoc* adjustments of the model parameters is necessary in order to fit experimental data. Naik-Nimbalkar *et al.* (2010) also applied steady-state RANS, but solved an additional equation for the scalar variance in order to predict the scalar fluctuations. Reasonable results were found after *ad-hoc* adjustment of the model parameters. Unsteady RANS with so-called scale-resolving models was investigated by Frank *et al.* (2009). The results gave quantitative information about the transient behavior of the scalar fluctuations, but did not successfully pass a comparison to experimental data in terms of the scalar RMS. LES has been applied among others by Hu & Kazimi (2006), Kuczaj *et al.* (2010) and Westin *et al.* (2008). LES was shown to be a promising technique for the prediction of turbulent mixing. Reasonable agreement with experimental data was found for sufficient grid resolution.

2.2. Pulsating flow in pipes

Pulsating flows in straight pipes have been studied in many publications due to the large amount of applications where pulsating flow can be encountered. The most well-known examples might be the pulsating blood flow caused by the heart beats. Pulsating flows are also found in combustion engines, piston pumps and hydraulic systems. In Carpinlioglu & Gundogdu (2001), a review of the work on pulsating flow in straight pipes can be found. The governing parameter for the pulsating flow is the Womersley number, defined as

$$\alpha = R\sqrt{\frac{\omega}{\nu}}, \tag{2.1}$$

where R is the radius of the pipe, ω is the angular frequency of the pulsation and ν is the kinematic viscosity of the fluid. The Womersley number gives the ratio between the oscillating inertial forces and the viscous forces; in the literature, it is also referred to as the normalized frequency parameter $\sqrt{\omega'}$. Depending on the Womersley number, three flow patterns have been identified. For low frequencies the flow is quasi-steady. In this region the flow is fully able to adjust to the pulsations and the resulting velocity profiles are equal to ones observed in stationary flow. The pressure and the velocity fluctuations are in phase. For very high pulsation frequency, the opposite is the case, i.e. the flow is not able to adjust to the pulsations, and the velocity fluctuations lag behind the pressure pulses by $90°$. The velocity profiles are substantially different from the stationary ones. For laminar flow, velocity peaks are located off the center of the pipe tending towards the pipe walls. In between these two regimes, there is an intermediate region where both phenomena are partly observed. The approximate limits between the regimes are given as $\alpha = 1.32$ as the upper limit for the quasi-steady region and $\alpha = 28$ as the lower limit for the inertia-dominated region (see Ohmi *et al.* (1981)). Another parameter is the Reynolds number based on the mean flow velocity. For high Reynolds number the flow is turbulent. Turbulent velocity

profiles in pulsating pipe flow have been measured among others by Dec *et al.* (1991), Shemer *et al.* (1985), Tu & Ramaprian (1983) and He & Jackson (2009). Scotti & Piomelli (2001) reported LES of pulsating turbulent channel flow. At high Reynolds and Womersley numbers, the velocity profiles are found to be rather flat, close to plug flow, since the momentum of the pulses is diffused quickly over the cross-section by the turbulence. At the same time, a developed boundary layer is not established due to the fast pulsations.

2.3. EGR mixing

The issue of EGR/Air mixing has been investigated in several studies. Experimental studies were performed by Green (2000), who measured instantaneous CO_2 distributions at the inlet ports of an engine by a Laser Absorption Spectroscopy technique and found large temporal variations. Wiliam & Dupont (2003) used Particle Image Velocimetry (PIV) and Planar Laser Induced Fluorescence (PLIF) in a generic test bench allowing for geometrical modifications. It was concluded that the use of a Venturi nozzle significantly improves the mixture quality, but also increases the pressure losses and that large cycle-to-cycle variations may occur. The latter implies that time or ensemble averages of the concentration are not sufficient for the characterization of the mixing process. Maiboom *et al.* (2009) showed that a non-uniform air/exhaust mixture may lead to higher NO_x and soot emissions.

On the computational side, several studies exist that all use experimental data for validation. In a study of Siewert *et al.* (2001), an intake manifold for a passenger car was improved in terms of EGR and air mixing, using both experimental and URANS methods. URANS computations have also been reported by Karthikeyan *et al.* (2011) and Yoshizawa *et al.* (2003) analyzing the effect of different mixer geometries on the EGR distribution. Ramanathan *et al.* (2011) coupled 3D-URANS computations directly to one-dimensional engine computations. The agreement with experimental data must, however, judged to be poor in terms of cylinder-to-cylinder EGR distribution (differences of more than 15%).

2.4. Contribution of this thesis

In general, the current computational research in the field of EGR non-uniformity rely mainly on URANS computations. The boundary conditions are either generic or taken from one-dimensional computations or on-engine measurements. However, no evaluation of the sensitivity to erroneous boundary conditions is available. Moreover, the inaccuracy due to the use of RANS turbulence models, which are calibrated for simple, stationary flow cases, has not been assessed. Apart from that, LES has not been applied to the problem of EGR mixing.

The main contribution of this thesis is therefore a systematical evaluation of modeling EGR mixing by LES. On the basis of these computations an evaluation of the accuracy of the results and the possible benefit compared to unsteady RANS computations is examined. Furthermore, an analysis in terms of the flow modes and flow

structures influencing the mixing quality is performed using advanced flow decomposition methods. The overall achievement is an increased understanding of the flow mechanisms that govern the mixing of air and EGR and the establishment methods of an LES method for accurate computation and analysis of such flows.

CHAPTER 3

Emissions of Internal Combustion engines

This chapter covers the basics regarding emission formation in ICE. First, the working principle of ICE is introduced and the description of engine cycles is treated. Thereafter, the problematic emissions and the most common approaches to their reduction are discussed shortly.

3.1. IC engine cycles

ICE convert chemical energy bound in fuel into mechanical energy. This is achieved by combustion of fuel delivering heat to the combustion gases entrapped in a cylinder. The increase of thermal energy of the gas results in a drastic pressure increase used to perform work on a piston through gas expansion. In this way the combustion gas works as the working medium. In order to produce work continuously this process has to be cyclic, i.e. the working medium has to return to its initial condition. The return to the initial condition in an ICE is obtained by an exchange of the working medium after each cycle (open cycle). The four-stroke engine is the most common ICE consisting of an intake stroke, a compression stroke, an expansion stroke and an exhaust stroke. One cycle consists therefore of two revolutions; one for generation of work and one for the gas exchange process.

Ideally, the engine cycle can be split up into four parts. Isentropic compression (1-2), combustion (2-3), isentropic expansion (3-4) and isochoric reversion (4-1). The combustion process can be assumed to be either isochoric or isobaric. Isochoric combustion corresponds to an infinitely fast combustion whereas isobaric combustion represents a very slow combustion process. The real combustion process is somewhere in between these processes, but usually closer to the isochoric process.

The isochoric assumption yields the ideal cycle for the constant-volume process, i.e. combustion takes places at a constant volume, which would be equivalent to an infinitely rapid heat supply. Further assumptions in this description are constant specific heats c_p and c_v and negligible heat and flow losses. The constant-volume-cycle is shown in the p-V-diagram (see Fig. 3.1), together with the constant-pressure-cycle shown in Fig. 3.2.

A real engine cycle will of course differ from the assumptions above and will rather resemble the cycle depicted in Fig. 3.3. This cycle is subject to fluid, thermodynamic and mechanical losses and comprises also the gas exchange cycle (see Dietsch & Klingebiel (2007) and Heywood (1988)).

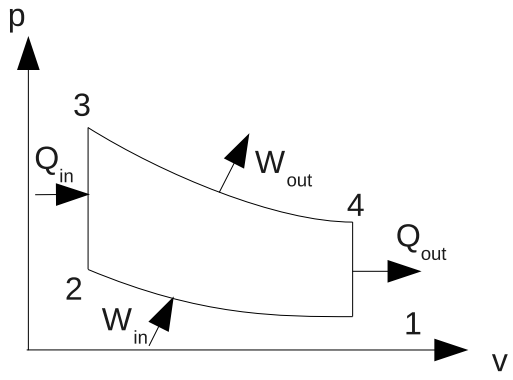

FIGURE 3.1. The ideal constant-volume cycle

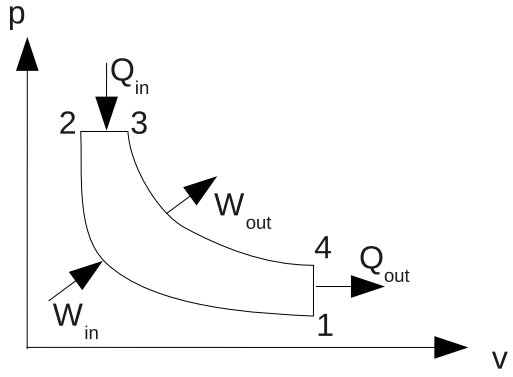

FIGURE 3.2. The ideal constant-pressure cycle

3.2. Combustion and emissions

Combustion is the chemical reaction that occurs between a fuel and an oxidizing agent that releases energy, usually in the form of heat and light. There are two generally different types of combustion in ICE, spark-ignited (SI) and compression-ignited (CI) combustion. The first one is usually associated with Otto- or gasoline engine, the latter with Diesel engines. In SI-combustion the flame starts at the spark and travels through the combustion chamber. Usually, the fuel is premixed with air in the intake manifold. In CI engines the fuel is injected directly into the combustion chamber, when high pressures and temperatures are already reached. The mixture of fuel and hot gases is then ignited by itself. Diesel engines can reach much higher efficiencies than gasoline engines, because higher pressure ratios can be reached. In gasoline engines the pressure ratio is limited by unwanted self-ignition of the fuel.

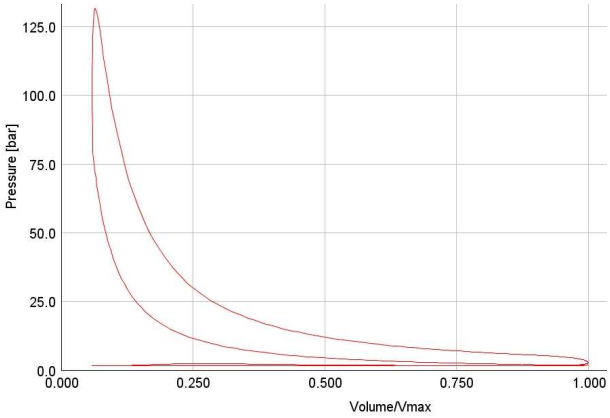

FIGURE 3.3. p-v-diagram for real engine (Courtesy of Simon Reifarth)

An important parameter for the combustion and the emission formation is the air/fuel ratio λ defined as

$$\lambda = \frac{m_{air}}{m_{fuel} \cdot Z}, \tag{3.1}$$

where m_{air} and m_{fuel} represent the mass of air and fuel participating in the combustion and Z is the stoichiometric factor of the fuel. If $\lambda = 1$, the amount of fuel corresponds exactly to the amount of air needed for complete combustion, i.e. all oxygen and fuel present in the combustion chamber are burned. If $\lambda > 1$, there is an excess of air, whereas $\lambda < 1$ represents an incomplete combustion due to too small amounts of air. Gasoline engines are usually operated at $\lambda = 1$, whereas Diesel engines usually have a higher $\lambda(> 1.2)$ in order to ensure complete combustion with fuel injection. For premixed combustion, λ is approximately constant over the combustion chamber whereas in a heterogeneous mixture λ may range locally from 0 to infinity, which is the case for direct fuel injection.

For SI-engines, the formation of emissions is highly dependent on λ. CI engines have very different emission characteristics as compared to SI engines. The emission formation in CI combustion is more dependent on the local λ.

Complete combustion at $\lambda = 1$ would produce only carbon dioxide (CO_2) and water. However, complete combustion is difficult to achieve and real combustion is always accompanied by unwanted emissions. Pollutant emissions regulated by legislation inside the EU, USA and Japan are: Particulate matter (PM), Nitric Oxides (NO_x), Hydrocarbons (HC) and Carbon monoxide (CO).

For Diesel combustion, the most problematic emissions are PM and NO_x. SI engines are primarily producing NO_x, CO, and HC emissions, whereas PM is not a big problem for SI engines.

NO_x is a common designation for the nitrogen oxides NO and NO_2. NO_x emissions in ICE are mainly formed as thermal NO_x according to the Zeldovic mechanism

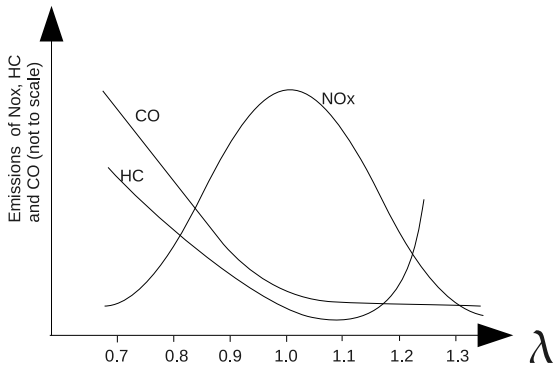

FIGURE 3.4. Dependency of emissions on λ for SI-engines (according to Heywood (1988))

(see e.g. Heywood (1988)). The formation of thermal NO_x is very temperature-dependent. Nitrogen (N_2) reacts with oxygen at temperatures higher than 2200 K. High combustion temperatures occur when λ is around 1, i.e. the reaction rate is high, since there are a lot of oxygen molecules available for the fuel to react with. For higher λ, the maximum combustion temperature and so the NO_x emissions are decreasing due to higher fuel dilution. The decrease of NO_x emissions is a challenge for both Diesel and SI engines, since NO_x emissions are the primary reason for photochemical smog in the presence of sun light.

CO occurs at low λ, due to incomplete oxidation. Thus, CO emissions are not problematic in Diesel engines. If CO is inhaled it binds with the red blood cells instead of oxygen, which can be lethal for high doses.

HC is a product of incomplete combustion at both high and low λ. HC is highly carcinogenic and is causing smog. HC is more problematic for SI engines.

Fig. 3.4 summarizes the λ-dependency of the different emissions for SI engines. CI engine emissions differ quantitatively from SI engines and are less dependent on λ. For example, NO_x emissions are about one order of magnitude greater in CI engines (see e.g. Heywood (1988)).

3.3. Reduction of emissions

Since emissions of pollutants are hazardous for the environment and humans, engine manufacturers had and will have to cope with drastic decreases of the legal emission limits. Fig. 3.5 shows the development of the allowed PM and NO_x emissions from 1992 to 2014. In less than 25 years, both NO_x and PM emissions have to be decreased by more than 95%.

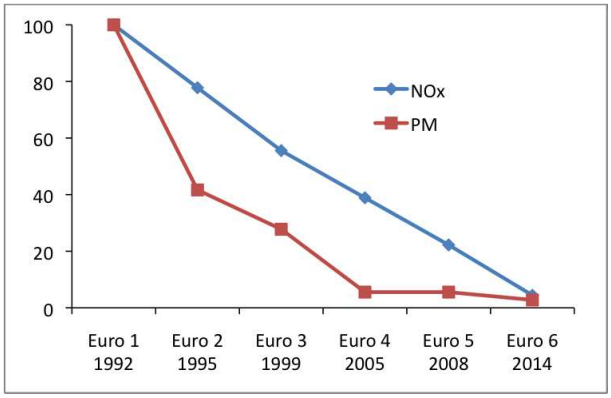

FIGURE 3.5. Emission limits on NO_x and PM from 1992 (Euro 1) until 2014 (Euro 6) in percentage of the limits given by Euro 1

Some of the most common and promising approaches to the problem are summarized in this section. EGR, which is the main focus of this thesis, is described more in detail.

3.3.1. *Alternativ combustion concepts*

Perhaps the most obvious way to reduce emissions is to obtain a cleaner and more complete combustion. A still fairly undeveloped approach is Homogenous Charge Compression Ignition (HCCI). It combines the principles of SI and Diesel engines as it uses a premixed fuel/air mixture and autoignition. This can be achieved by injecting the fuel very early during the compression stroke. Advantages with this approach are dramatically improved NO_x and PM emissions due to a more homogenous combustion avoiding high peak temperatures. However, the combustion phasing is difficult to control, since it is determined solely by the fuel mixture and the compression ratio (see Stanglmaier & Roberts (1999)).

A proposal to control the autoignition event is Partially Premixed Compression Ignition (PPCI). The idea is to control the injection event such that the combustible mixture is not completely homogeneous at the time of ignition, rather only 'partially' premixed. This leads to occurrence of richer and leaner regions within the combustion chamber, causing the combustion to start at several regions simultaneously, thus slowing down the combustion and the heat release (see Stanglmaier & Roberts (1999)).

The approach of stratified combustion is to use and control fuel injection in SI-engines in such way that there are different layers within the combustion chamber with richer mixture close to the spark and leaner mixture as the flame is spreading. High combustion temperatures can thereby be avoided. These techniques are very difficult to control and are still in the development phase.

3.3.2. *After-treatment*

After-treatment of exhaust gases denotes the reduction of emissions contained in the exhaust gases after combustion. This can be achieved by catalyzers, filters and/or reducing agents. An oxidation catalyst is able to significantly lower emissions of CO and HC. A three-way catalyst further improves the reduction of NO_x emissions. However, a prerequisite for efficient operation of the three-way-catalyzer is that $\lambda \sim 1$. Its use is therefore limited to SI engines. An additional way to significantly lower NO_x emissions is Selective Catalytic Reduction (SCR). A reducing agent, most often ammonia (NH_3) formed from urea, is injected into the exhaust gases and selectively oxidizes with the oxygen contained in the nitrogen oxides (see Dietsch & Klingebiel (2007)). The disadvantage with SCR is that urea has to be transported in the vehicle and refilled. Furthermore, there are issues due to crystallization of urea in cold start, that can cause blockage of the exhaust piping.

3.3.3. *Exhaust Gas Recirculation (EGR)*

One of the most efficient ways to reduce NO_x emissions is to avoid high peak combustion temperatures during combustion by EGR. A portion of the exhaust gases is recirculated and mixed with the intake air prior to combustion. Exhaust gases contain less oxygen and more carbon dioxide than pure air. Therefore, the introduction of exhaust gases into the intake air leads to a decreased oxygen concentration of the combustion gases compared to operation without EGR. Furthermore, uncooled EGR contains also water vapor resulting from the combustion process. Often EGR is cooled beyond the condensation temperature prior to the introduction into the intake air in order to avoid condensed water in the cylinders.

EGR affects the combustion due to several effects that were summarized in Maiboom *et al.* (2008). The dilution with CO_2 and other combustion products slows down the reaction rate between fuel and oxygen, since there are less oxygen molecules available for the combustion. Thus, the local peak temperatures in the flame are decreased. Moreover, the heat capacity of the mixture is increased due to the presence of three-atomic CO_2 and water vapor in the mixture, i.e. with the same energy released from the combustion the temperature is lower. Other effects are consequences of the slower combustion. The combustion is delayed and is therefore pushed further into the expansion stroke, where the lower pressure leads to lower combustion temperatures. Also the delayed ignition of the mixture observed with EGR contributes to this effect and leads to a more premixed combustion, which decreases local temperature peaks.

EGR is mainly used in CI engines. However, EGR is also promising in SI engines for NO_x reduction in regimes where catalyzers do not work and for decreasing throttle losses (if EGR is present the throttle has to be opened further). Recently, Chauvet & Dimitrova (2008) showed that the addition of cooled EGR in SI-engines at high loads

can result in a decrease of fuel consumption up to 20% since excessive over-fueling needed for the reduction of the exhaust temperatures is avoided [1].

EGR can be achieved internally by valve overlap or externally through a connection between the exhaust pipe and the intake manifold, where an EGR valve controls the EGR flow. In combination with a turbocharger, it is possible to introduce the exhaust gases upstream or downstream of the turbocharger. The first is referred to as long-route EGR, the latter as short-route EGR. Even though long-route EGR offers some advantages in terms of engine efficiency, short-route is still the state-of-the-art, mainly because the introduction of exhausts and soot into the compressor is not desirable.

Limits on the amount of EGR are given by misfire due to lack of oxygen, resulting in higher HC emissions (see Schwarz *et al.* (1988)). Furthermore, high EGR rates will decrease the engine efficiency through pump losses.

Another issue regarding the use of EGR is the mixing quality between exhaust gas and air, which is the topic of this thesis. Non-uniform mixtures of air and exhaust gases are problematic, since they will influence the engine performance and emissions. The mixture can be non-uniformly distributed among the cylinders as well as inside the combustion chamber. The non-uniformity can lead to misfire and high soot emissions for locally large EGR concentration and increased NO_x emissions for small EGR concentration.

Recently, Choi *et al.* (2011) have also investigated the use of intentionally stratified in-cylinder EGR concentration. The idea is similar to the previously described stratified combustion. It aims on achieving layers of different EGR distribution in the combustion chamber with higher EGR content close to the injector in order to avoid high peak combustion temperatures and lower EGR content far away from the injector in order to avoid quenching and soot formation. Due to the difficulties of controlling these processes, this method is still in development.

[1] For SI engines at high loads, it is common to inject more fuel than actually needed in order to avoid high exhaust temperatures that can damage the catalyzer

CHAPTER 4

Turbulence and turbulent mixing

Turbulence characterizes the chaotic and unsteady motion found in most technical fluid flow applications. Turbulence occurs when the inertial forces are much greater as compared to the viscous ones. Thus, the most important parameter of turbulence is the Reynolds number giving the ratio of the inertial forces to the viscous forces,

$$Re = \frac{\mathscr{U} \cdot \mathscr{L}}{\nu}, \tag{4.1}$$

where $\mathscr{U}$ is a characteristic velocity and $\mathscr{L}$ a characteristic length of the flow. $\mathscr{L}$ corresponds to the largest scales of the flow. The definition of the largest length scale of the flow is rather subjective and case-dependent, e.g. in pipe flow it is the hydraulic pipe diameter, in jet flow it is the nozzle diameter and in flows over wings it is the chord of the wing. If the Reynolds number is high enough, the flow is turbulent, i.e. even in simple flow situations, as pipe flow, the velocity field can be highly unsteady and chaotic.

Characteristic for turbulence is the presence of fluid motion within a large range of scales. An increase of the Reynolds number will increase the range of scales of the turbulent motions, i.e. with increasing Reynolds number, the smallest scales, at which dissipation occurs, are decreasing.

This chapter introduces Kolmogorov's hypotheses, used to estimate the smallest scales of the turbulent motions and the energy transport from larger to smaller scales. Corresponding considerations are introduced for the passive scalar mixing, based on Batchelor's ideas.

4.1. The energy cascade and Kolmogorov's hypotheses

Important facts concerning turbulence are the existence of a broad range of scales in the fluid motion and the transport of energy from larger to smaller scales, i.e. large eddies break up into smaller eddies. However, the bulk of the kinetic energy is contained in the largest scales, governed by the boundary conditions. At sufficiently high Reynolds numbers, the statistics of the smallest scales can be assumed to be isotropic and independent of the boundary conditions, i.e. all information about direction is lost in the break-up process. From these arguments it can be concluded that the small scales are universal, i.e. the small scales have a similar behavior in all flow realizations.

The energy transfer starts at the largest scales and continues until viscous dissipation takes over. Since viscous effects occur mainly at the smallest scales, an estimation

of the smallest scales can be made from dimensional analysis following Kolmogorov's first hypothesis. Kolmogorov's first hypothesis states that at sufficiently high Reynolds number, the smallest scales are only dependent on the dissipation rate ϵ and the kinematic viscosity ν (see Kolmogorov (1991)[1]). From dimensional arguments, it can be found that the only possible way to form length, velocity and time scales from ϵ and ν are

$$\eta = (\frac{\nu^3}{\epsilon})^{\frac{1}{4}} \tag{4.2}$$

$$u_\eta = (\epsilon\nu)^{\frac{1}{4}} \tag{4.3}$$

$$\tau_\eta = (\frac{\nu}{\epsilon})^{\frac{1}{2}}. \tag{4.4}$$

When in equilibrium, the energy transfer between the scales must equal the dissipation rate. At intermediate scales ($\mathscr{L} >> l_o >> \eta$), too small for the boundaries to affect their behavior, and too large for viscous effects to take place, the energy transfer can only depend on the dissipation rate ϵ. This is Kolmogorov's second hypothesis (see Kolmogorov (1991)). This range is called the inertial subrange.

Statistics of turbulence are often analyzed in the wave-number or the frequency domain. The energy spectrum $E(k)$ gives the distribution of turbulent kinetic energy over the range of frequencies or wave numbers k of the turbulent scales. The length scale and the wave number are related through $k = 2\pi/l$.

From Kolmogorov's second hypothesis and dimensional analysis the following relation is found:

$$E(k) \propto \epsilon^{2/3} k^{-5/3}, \tag{4.5}$$

which gives the slope of the energy spectrum.

A qualitative sketch of the energy spectrum is shown in fig. 4.1. The inertial subrange has a slope of $k^{-5/3}$ up to the smallest scales given by $2\pi/\eta$. For a more detailed description of turbulence the reader is referred to e.g. Pope (2008).

4.2. Turbulent mixing

Turbulent mixing designates the mass transport due to turbulence. In general, reactive mixing can be distinguished from passive mixing. In reactive mixing the mass transport influences the flow properties, whereas in passive mixing, as the name indicates, the transport is passive, i.e. it does not influence the flow field. This thesis will only consider passive mixing. The mechanisms governing the passive mixing are advection and molecular diffusion. Advection is the transport of mass by the flow and particularly by turbulence. Molecular diffusion is the process caused by motions on the molecular level (Brownian motion). In fluids, molecules are constantly moving in all directions and interacting with other molecules. In the presence of two species this motion gives a net transport from one species to the other one. In the absence of high temperature and pressure gradients, molecular diffusion acts against the gradient

[1] Translation of russian original from 1941

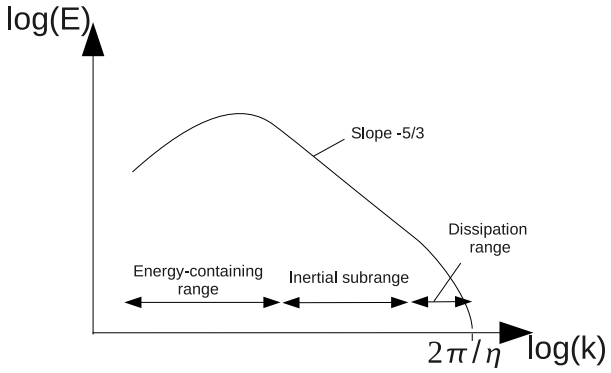

FIGURE 4.1. The turbulent energy spectrum

of the transport quantity and the resulting flux is proportional to the gradient of the transport quantity (concentration). Thus, the flux J_i can be expressed by Fick's law,

$$J_i = -\kappa \frac{\partial \phi}{\partial x_i}, \tag{4.6}$$

where κ is the diffusion coefficient and ϕ is some transported scalar (e.g. a concentration)[2].

For high Reynolds numbers, molecular diffusion is much slower than advection. Thus, molecular diffusion can only act on the smallest scales. An important dimensionless number is the Schmidt number,

$$Sc = \frac{\nu}{\kappa}, \tag{4.7}$$

representing the ratio between momentum diffusivity and molecular diffusivity. Typical values for Sc are approximately unity for gases and in the order of 1000 for liquids. The value of the Schmidt number is temperature and pressure dependent. However, this is neglected throughout this thesis.

In the case of $Sc < 1$, the smallest scales of the transport scalar are diffused faster than those of the velocities. The energy spectrum of the scalar fluctuations must therefore have a lower cut-off wave number as compared to the velocity spectrum. $Sc > 1$ displays the opposite behavior and much smaller scales are present in the scalar spectrum (greater wave lengths). The slope of the energy spectrum is -1 for wave lengths beyond the Kolmogorov scales, which can be shown from dimensional arguments. For smaller wave lengths, where diffusion is negligible, the scalar spectrum shows the same behavior as the velocity spectrum. Fig. 4.2 shows the theoretical scalar spectrum for the different Schmidt number regimes.

[2]This is equivalent to heat conduction, which is the reason why the temperature in incompressible flows can be treated as a passive scalar

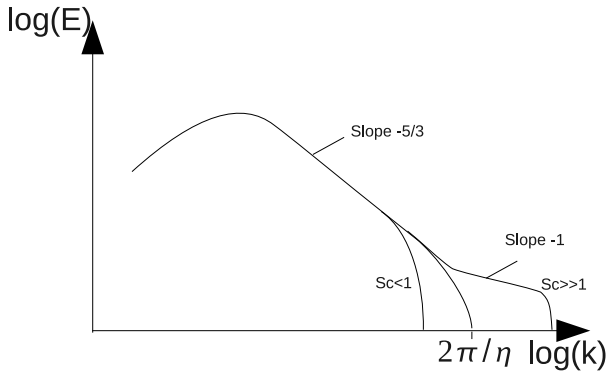

FIGURE 4.2. The scalar energy spectrum

This behavior was first predicted by Batchelor (1959) and Batchelor *et al.* (1959), who also derived the smallest scales of the scalar spectrum, which differ from the Kolmogorov scales for $Sc \neq 1$. The Batchelor scales can be expressed in terms of the Kolmogorov scales and the Schmidt number as

$$\lambda_B = \left(\frac{\nu\kappa^2}{\epsilon}\right)^{1/4} = \eta \cdot Sc^{-1/2},\ for\ Sc \gtrsim 1 \tag{4.8}$$

and

$$\lambda_B = \left(\frac{\kappa^3}{\epsilon}\right)^{1/4} = \eta \cdot Sc^{-3/4},\ for\ Sc < 1. \tag{4.9}$$

CHAPTER 5

Computation of turbulent mixing

In order to compute turbulent mixing process, the equations governing the flow (and the turbulence) have to be solved. Additionally to the flow equations, a transport equation for the mixing scalar is solved. Several approaches to the numerical solution of these equations have been proposed. The approaches can be categorized into three groups; Direct numerical simulation (DNS), Large eddy simulations (LES) and Reynolds averaged Navier-Stokes (RANS) computations.

In DNS all scales are resolved, thus no modeling is needed. This is, however, very computational expensive since the smallest scales decrease with increasing Reynolds number (see Chapter 4). It can be shown that the computational costs scale with the Reynolds number as Re^3 making DNS unfeasible for flows with high Reynolds numbers.

LES is an approach in order to circumvent the difficulties in DNS by resolving only the scales that carry the major part of the turbulent kinetic energy. The effect of the unresolved scales on the resolved scales is modeled by a sub-grid-scale (SGS) model. In a RANS, the equations for the ensemble-averaged equations are solved, i.e. all scales of turbulent motion are modeled.

This chapter introduces the governing flow equations. Thereafter, the LES and RANS models handling turbulence and turbulent mixing are described. Finally, the boundary conditions and the numerical methodology are discussed.

5.1. Governing equations

The Navier-Stokes equations for a compressible flow, based on conservation of mass, momentum and energy are:

$$\frac{\partial \rho}{\partial t} + \frac{\partial}{\partial x_j}\left[\rho u_j\right] = 0 \tag{5.1}$$

$$\frac{\partial}{\partial t}\left(\rho u_i\right) + \frac{\partial}{\partial x_j}\left[\rho u_i u_j + p\delta_{ij} - \tau_{ji}\right] = 0, \quad i = 1, 2, 3 \tag{5.2}$$

$$\frac{\partial}{\partial t}\left(\rho e_0\right) + \frac{\partial}{\partial x_j}\left[\rho u_j e_0 + u_j p + q_j - u_i \tau_{ij}\right] = 0, \tag{5.3}$$

where ρ is the density, u_i is the velocity component in i-direction, e_o is the total specific energy defined as $e_o = e + \frac{1}{2}u^2$, e is the internal specific energy, p is the static pressure, τ_{ij} is the viscous stress tensor and q_j is the heat flux. In a Newtonian fluid

the viscous stresses are proportional to the strain rate. With the definition of the strain rate tensor

$$S_{ij} = \frac{1}{2}(\frac{\partial u_i}{\partial x_j} + \frac{\partial u_j}{\partial x_i}), \tag{5.4}$$

τ_{ij} can be written as

$$\tau_{ij} = 2\mu(S_{ij} - \frac{1}{3}S_{kk}\delta_{ij}). \tag{5.5}$$

Moreover, for the compressible form of the Navier-Stokes equations, an equation of state is necessary in order to close the equation system. In moderate temperature ranges, the ideal gas equation gives sufficient accuracy:

$$p = \rho RT, \tag{5.6}$$

where R is the specific gas constant and T is the temperature.

As mentioned in the previous chapter, the passive scalar is governed by the advection-diffusion equation. In general, the scalar equation is written as

$$\frac{\partial \rho\phi}{\partial t} + \frac{\partial \rho u_i \phi}{\partial x_i} = \frac{\partial}{\partial x_i}\rho\kappa\frac{\partial \phi}{\partial x_i}. \tag{5.7}$$

Assuming a constant Schmidt number, which is defined as

$$Sc = \frac{\mu}{\rho\kappa}, \tag{5.8}$$

and a constant viscosity $\mu = const.$, equation (5.7) can be rewritten as

$$\frac{\partial \rho\phi}{\partial t} + \frac{\partial \rho u_i \phi}{\partial x_i} = \frac{\mu}{Sc}\frac{\partial^2 \phi}{\partial x_i \partial x_i}. \tag{5.9}$$

By using partial derivation and the continuity equation this simplifies to:

$$\frac{\partial \phi}{\partial t} + u_i\frac{\partial \phi}{\partial x_i} = \frac{\nu}{Sc}\frac{\partial^2 \phi}{\partial x_i \partial x_i}, \tag{5.10}$$

with $\nu = \mu/\rho$.

Normalizing the variables u_i, x_i and t by the velocity, length and time scales of the flow as,

$$u_i^+ = \frac{u_i}{\mathscr{U}},\ x_i^+ = \frac{u_i}{\mathscr{L}},\ t^+ = t\frac{\mathscr{U}}{\mathscr{L}}, \tag{5.11}$$

and inserting into eq. (5.10) yields the scalar equation in its non-dimensional form:

$$\frac{\partial \phi}{\partial t^+} + u_i^+\frac{\partial \phi}{\partial x_i^+} = \frac{1}{Re \cdot Sc}\frac{\partial^2 \phi}{\partial x_i^+ \partial x_i^+} \tag{5.12}$$

The product of the Reynolds number and the Schmidt number in eq. (5.12) is also known as Peclet number $Pe = Re \cdot Sc$. From (eq. 5.12), it is obvious that the diffusion term is small when the Peclet number is large.

5.2. Modeling of turbulence and turbulent mixing

As mentioned earlier in this chapter, DNS of turbulent flows at high Reynolds numbers are not feasible due to the high demands on computational resources. For high Schmidt numbers this problem is even more severe due to the Batchelor scale (see eq. (4.8)) being even smaller as compared to the Kolmogorov scale. Thus, it is necessary to introduce models in order to facilitate less computational demanding simulations.

5.2.1. *RANS*

Ensemble-averaging of the Navier-Stokes equation yields the so called Reynolds equations. The Reynolds equations differ from the Navier-Stokes equations through the occurrence of an additional unclosed term, the so called Reynolds stresses given by $\overline{u_i' u_j'}$, where the overbar denotes the averaging of the quantity below. For more details see e.g. Pope (2008). The Reynolds stress term has to be modeled. During the past five decades, many turbulence models have been suggested throughout literature. However, none of the proposed models are universally applicable to all flow problems (see e.g. Schäfer (1999)).

A commonly used RANS model is the k-ϵ-model, which will be presented here. The k-ϵ-model is based on the turbulent-viscosity hypothesis (Boussinesq's hypothesis), assuming an analogy between the Reynolds-stresses and the viscous stresses in an Newtonian fluid (see equation (5.5)):

$$\overline{u_i' u_j'} - \frac{2}{3} k \delta_{ij} = -2\nu_t \overline{S}_{ij}, \tag{5.13}$$

where ν_t is called the turbulent viscosity. However, there is an important difference when compared with the molecular viscosity; ν_t is not a fluid property, it is a property of turbulence. Thus, it is a function of position (and time). The specification of ν_t is the subject of all turbulent-viscosity-models. In the case of the k-ϵ-model, transport equations for k and ϵ are formulated on the basis of semi-empirical relations (see Launder & Spalding (1974)). The equations are written as:

$$\frac{\partial}{\partial t}(\rho k) + \frac{\partial}{\partial x_i}(\rho k u_i) = \frac{\partial}{\partial x_j}\left[\left(\mu + \frac{\mu_t}{\sigma_k}\right)\frac{\partial k}{\partial x_j}\right] + G - \rho\epsilon \tag{5.14}$$

$$\frac{\partial}{\partial t}(\rho \epsilon) + \frac{\partial}{\partial x_i}(\rho \epsilon u_i) = \frac{\partial}{\partial x_j}\left[\left(\mu + \frac{\mu_t}{\sigma_\epsilon}\right)\frac{\partial \epsilon}{\partial x_j}\right] + C_{\epsilon 1}\frac{\epsilon}{k}G - C_{\epsilon 2}\rho\frac{\epsilon^2}{k}, \tag{5.15}$$

with

$$G = \mu_t \left(\frac{\partial u_i}{\partial x_j} + \frac{\partial u_j}{\partial x_j}\right)\frac{\partial u_i}{\partial x_j}. \tag{5.16}$$

The turbulent viscosity is evaluated as:

$$\nu_t = C_\mu \frac{k^2}{\epsilon}. \tag{5.17}$$

The model constants are: $C_\mu = 0.09$, $\sigma_k = 1.0$, $\sigma_\epsilon = 1.3$, $C_{\epsilon 1} = 1.44$ and $C_{\epsilon 2} = 1.92$.

Thus, the k-ϵ-model needs five model constants that are calibrated against simple flow cases. The model can therefore not be expected to be valid in complex geometries with high degrees of anisotropy.

Similar to the Reynolds stresses, an additional term occurs when applying ensemble-averaging to the passive scalar equation (5.10). The resulting equation is:

$$\frac{\partial \overline{\phi}}{\partial t} + \overline{u_i}\frac{\partial \overline{\phi}}{\partial x_i} = \frac{\nu}{Sc}\frac{\partial^2 \overline{\phi}}{\partial x_i^2} - \frac{\partial \overline{u_i'\phi'}}{\partial x_i} \tag{5.18}$$

The last term in eq. (5.18) is the turbulent flux vector, a term that is unknown and therefore has to be modeled. The most basic approach is the so-called Gradient Diffusion Model (GDM). This model relies on the assumption that the turbulent flux vector is aligned with the scalar gradient, analogous to molecular diffusion:

$$\overline{u_i'\phi'} = -\kappa_t \frac{\partial \overline{\phi}}{\partial x_i}, \tag{5.19}$$

where κ_t is computed from the turbulence characteristics delivered by the turbulence model. For the $k-\epsilon$ model it is

$$\kappa_t = \frac{\nu_t}{Sc_t} = \frac{C_\mu}{Sc_t}\frac{k^2}{\epsilon}, \tag{5.20}$$

containing the turbulent Schmidt number Sc_t, a model constant. Commonly, an empirical value of $Sc_t = 0.9$ is used. However, it should be noted that the assumption of gradient-diffusion is only valid for isotropic turbulence. Even in simple shear flows, deviation from this assumption can be observed (see Pope (2008)).

An improvement of the GDM is the Generalized Gradient Diffusion Model (GGDM). It includes the effects of non-gradient diffusion by involving the Reynolds stresses as,

$$\overline{u_i'\phi'} = -C_h \overline{u_i'u_j'}\frac{k}{\epsilon}\frac{\partial \overline{\phi}}{\partial x_j}, \tag{5.21}$$

where C_h is a model constant, usually 0.3. The product of the Reynolds stress tensor and the scalar gradient in eq. (5.21) provides a flux vector that is not aligned with the scalar gradient, if there is significant anisotropy present in the flow. The GGDM originates from observations in jet flows, where entrainment of the surrounding fluid into the jet occurs, which cannot be predicted by the GDM. The model constant C_h is calibrated from these observations.

Common for RANS-models are the numerous assumptions and empiricism needed in order to close the equations. Some of these assumptions, as the gradient diffusion assumption, are not justified by physics. Their only justification is the lack of a better assumption and/or simplicity. The big advantage with the RANS approach is that all turbulent fluctuations are filtered out and thus do not have to be resolved. This in turn leads to low computational costs.

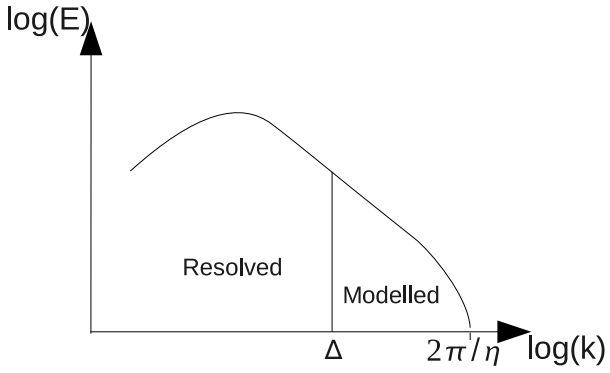

FIGURE 5.1. The turbulent energy spectrum for LES

5.2.2. *LES*

DNS is computationally expensive for high Reynolds numbers and RANS is lacking generality due to the numerous models and assumptions needed. Large Eddy Simulation (LES) was developed in order to overcome the shortcomings of RANS and avoiding being as computational expensive as DNS. In LES, the large energy containing scales (or eddies) are resolved, whereas the effect of the unresolved scales on the resolved scales is modeled. This is possible because the small scales have a universal and isotropic character (see Chapter 4). Hence, the small scales are rather independent of the boundary conditions.

The principle of LES is illustrated in Fig. 5.1. The large scales are directly resolved, whereas the scales smaller than a filter width $\tilde{\Delta}$ are removed by some filtering operation. This spatial filtering operation can be performed explicitly or implicitly. The filtering of the Navier-Stokes equations leads to residual stresses τ^r on the right hand side of the momentum equation, similar to the Reynolds stresses for RANS. The residual stresses have to be modeled in a way, that reflects the impact of the small scales on the resolved scales. Models for τ^r have to satisfy the following characteristics:

- They have to mimic the dissipation, that occurs at the small scales. I.e. they have to drain energy from the large scales.
- At the limit $\tilde{\Delta} \rightarrow 0$, the residual stresses should vanish since approaching DNS.
- Ideally, backscatter should be allowed, i.e. intermittent transport of energy from the unresolved to the resolved scales.

One of the simplest and first models proposed is the Smagorinsky model, a model introducing an eddy-viscosity ν_r analogous to the turbulent viscosity in RANS. The

residual stresses are then written:

$$\tau_{ij}^r = -2\nu_r \tilde{S}_{ij} \tag{5.22}$$

where the tilde designates the filtering operation. ν_r is modeled as

$$\nu_r = (C_s \tilde{\Delta})^2 \tilde{S}, \tag{5.23}$$

with $\tilde{S} = \sqrt{2\tilde{S}_{ij}\tilde{S}_{ij}}$ and the Smagorinsky parameter $C_s = 0.17$, which is derived from homogenous isotropic turbulence.

If a passive scalar equation is solved along with the Navier-Stokes equations, the filtering process gives sub-grid fluxes j_i^r analogous to the sub-grid stresses. The sub-grid fluxes can for example be modeled by assuming gradient diffusion:

$$j_i^r = \frac{\nu_r}{Sc_t} \frac{\partial \tilde{\phi}}{\partial x_i} \tag{5.24}$$

Shortcomings of the Smagorinsky model are due to the constant parameter C_s, which is not generally valid, and in particular close to walls or in laminar regions. Furthermore, eddy-viscosity models with $\nu_r > 0$ do not allow for energy transfer from the small scales to the large scales (backscatter). Dynamic models adjust C_s locally assuming an asymptotic behavior of the model. By applying two filter operations with different filter widths, an extrapolated value of SGS can be obtained. The goal is then to find $C_s(x,t)$ that gives the best representation of the residual stresses on both filter levels. A modeling approach allowing for backscatter is the scale-similarity model, which is based on an extrapolation of the smallest resolved scales to the largest unresolved scales.

Another approach applying a somewhat different philosophy is the implicit modeling of the unresolved scales. The underlying idea is that the use of differencing schemes in finite volume methods is inevitably connected with truncation errors. The effect of the truncation error is in turn similar to the effect of the residual stresses, i.e. it is dissipative and tends to zero as the filter width is decreasing. Thus, instead of adding additional dissipation by introducing a model, the numerical dissipation can be used. Furthermore, it can be argued that the exact amount of dissipation is not important, as long as the resolution is good enough to resolve a large part of the inertial subrange, because the energy transfer from large to small scales in this region is independent of viscosity (and therefore also of numerical viscosity) according to Kolmogorov's hypothesis.

Advantages with the implicit approach are its simplicity and straight-forward formulation. The absence of an explicit model also leads to reduced computation times. Furthermore, it is superior to e.g. the Smagorinsky model in laminar regions or close to the walls, since Smagorinsky is too dissipative in these regions (C_S should be zero in these regions). In pulsating flow or in very complex geometries, where high anisotropy occurs, the modeling assumptions of many sub-grid scale models are not valid. Thus, implicit LES with high mesh resolution seems to be more adequate for these cases. Drawbacks with the implicit approach are higher grid-dependency (i.e.

requiring fine grid resolution) and the lack of information about the unresolved turbulence properties. The latter is significant if it is necessary to model processes that occur at scales smaller than the resolved scales.

5.3. Boundary conditions

Another important aspect in flow computations as well as an important error and uncertainty source is the specification of the boundary conditions. This is particularly true for engine computations, where the correct boundary conditions to a great extent are difficult to measure or compute due to pulsations and moving boundaries, e.g. cylinder valves.

Basically, the boundaries can be divided into walls and open boundaries, such as inlets and outlets. The specification of the velocity on the walls is rather straightforward, since infinitely close to a wall the fluid has to have the same velocity as the wall, i.e. $u = u_{wall}$. More difficult is the boundary condition for the energy equation at the wall. One possibility is the assumption of adiabatic walls, equivalent to a zero-gradient condition on the temperature, i.e $\frac{\partial T}{\partial x_i} n_i|_{wall} = 0$. However, if high temperature gradients between the fluid and the wall are present, there will be a significant heat transfer between the fluid and the wall. This heat transfer is difficult to estimate, since the temperature of the wall is not known nor the transient heat-flux into the wall. Another possibility is the assumption of a constant wall temperature $T|_{wall}$=const, which might be estimated e.g. from measurements of the time-averaged wall temperature. The true heat transfer may lie somewhere in between the adiabatic and the constant temperature conditions. For the simulation of the concentration, a zero-gradient condition is applied at the walls, $\frac{\partial \phi}{\partial x_i} n_i|_{wall} = 0$, i.e. no mass transfer is allowed through the wall.

In stationary compressible flow problems, it is often most suitable to specify the mass flow rate or the velocity on the flow inlets together with the inlet temperature. On the outlet, often a constant pressure condition or non-reflective pressure condition is used. In the case of an inlet manifold, however, the mass flow through the outlets is changing drastically in time. Moreover, each valve is closed during large parts of the cycle allowing no flow through the cylinder ports. A small error in the time-dependent pressure on the outlet could therefore result in a significant flow through the valve at times where the valve is closed. Thus, it is beneficial in these cases to set the mass flow on the outlets and set the pressure and the temperature on the inlets. The time-dependent mass flow at the outlets can be estimated from one-dimensional engine computations. The time-dependent pressure on the inlets can be measured fairly easy directly on the engine or also be estimated from one-dimensional models. When the pressure is set on the inlet (together with the temperature), the velocity is the only free variable on the inlet. For stability, it is necessary to fix the direction of the inlet velocity, normally orthogonal to the inlet surface. For the scalar, one chooses usually to set $\phi = 1$ on one inlet and $\phi = 0$ on the other inlet, i.e. $\phi = 1$ means a concentration of 100% and $\phi = 0$ means 0%. On the outlets, a zero-gradient condition is used for the scalar.

5.4. Numerics

The first task in all numerical simulations of a flow problem is the mesh generation. The mesh can be either structured or unstructured. A mesh is called structured if the distribution of nodes can be expressed as some function of the space coordinates. In complex geometries, structured meshes are difficult or impossible to achieve. In these cases, one often uses unstructured meshes, in which the node distribution is rather random, e.g. as a result of an automatic grid generator. Thereafter, the discretization scheme needs to be formulated, transforming the continuous equations onto the discrete mesh. In time-dependent problems a temporal discretization is needed as well. Furthermore, in order to numerically solve the discretized equations, a solution algorithm has to be defined. The approaches chosen to perform the work presented in this thesis are further described in this section.

5.4.1. *Discretization*

The discretization method used throughout this study is the finite-volume-method. Other methods available are discretization by finite differences and finite elements. Advantages of the finite volume method are the relatively simple implementation and broad applicability, e.g. for complex geometries. A short introduction will be given here for the example of the passive scalar equation (eq. (5.7)). Integrating the equation over an arbitrary control volume V and applying Gauss' theorem delivers

$$\int_V \frac{\partial \phi}{\partial t} dV + \int_S (u_i \phi) n_i dS = \int_S (\kappa \frac{\partial \phi}{\partial x_i}) n_i dS, \tag{5.25}$$

where S is the surface of the control volume and n_i are the components of the surface normal vector(see Schäfer (1999)). Three different terms can be identified; a temporal integral, an advective flux and a diffusive flux. The discretization of the temporal and spatial terms will be treated separately.

5.4.1a. *Spatial discretization.* For simplicity, the methods are illustrated by assuming a two-dimensional Cartesian mesh with the notations shown in Fig. 5.2. The control volume is split up into the plane sections defined by the grid points.[1] The purpose of the discretization is to approximate the integrals by values of ϕ on the grid points. In order to achieve this, the first step is the approximation of the integral by assuming a constant value of ϕ and $\frac{\partial \phi}{\partial x_i}$ over the surfaces of the control volume.

$$\int_S (u_i \phi) n_i dS \approx \sum_c u_i \phi_c n_{ci} \delta S_c \tag{5.26}$$

and

$$\int_S (\kappa \frac{\partial \phi}{\partial x_i}) n_i dS \approx \sum_c \kappa \left(\frac{\partial \phi}{\partial x_i} \right)_c n_{ci} \delta S_c \tag{5.27}$$

where the index c denotes the values on the middle of the surfaces.

[1] In two dimensions, volumes obviously turn into surfaces and surfaces into curves, but in order to be consistent with the three-dimensional problem the original designations are kept

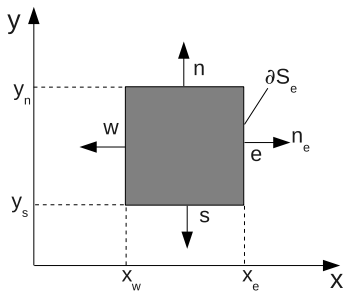

FIGURE 5.2. Control volume with designations - Sides s,w,n are designated in analogy to side e

The next task is to express ϕ_c and $\left(\frac{\partial \phi}{\partial x_i}\right)_c$ by the values of the neighboring grid nodes, which is the definition of the spatial differencing scheme. A simple scheme of second order for the advective term is the central differencing scheme. It is identical with a linear interpolation of the ϕ_c by the two neighboring nodes. For instance;

$$\phi_e \approx \phi_P + \frac{\phi_E - \phi_P}{x_E - x_P} \frac{x_e - x_P}{x_E - x_P} \tag{5.28}$$

In spite of its simplicity and formal accuracy of second order, the CDS (without modification) is often useless in practical application to complex geometries, since it allows for unphysical oscillations when sharp gradients occur. It is therefore necessary to introduce damping in the form of artificial dissipation, flux-limiters or filters.

Another possibility is the use of upwind schemes. The simplest upwind scheme is the following,

$$\phi_e = \phi_P, \quad for\ \dot{m}_e > 0 \tag{5.29}$$

$$\phi_e = \phi_E, \quad for\ \dot{m}_e < 0 \tag{5.30}$$

When applying an upwind-scheme, information can only travel in the direction of the mass flow making oscillations impossible. Upwind schemes are especially useful in supersonic flows. However, for subsonic flows, upwind schemes tend to be too dissipative, since the interpolation error is of first order. It is also possible to build combinations of CDS and upwind schemes by using some mixing function.

For the computations of the complex geometries with unstructured and comparably irregular meshes, a flux-limited CDS was used for stability. For the T-junction cases with structured uniform meshes, the pure CDS was sufficiently stable.

The discretization of the diffusive fluxes is less problematic. The spatial derivative is most commonly approximated by central differences

$$\left(\frac{\partial\phi}{\partial x}\right)_e \approx \frac{\phi_E - \phi_P}{x_E - x_P}, \tag{5.31}$$

assuming linearity between the two neighboring points. This scheme gives an accuracy of second order and there are no limitations due to oscillations as for the advective schemes.

5.4.1b. *Temporal discretization.* Similarly to the spatial discretization, the time domain is split up into finite time steps. A basic difference as compared to the spatial discretization is that the values of ϕ at a time t^n (where the superscript denotes the current time step) can only depend on values of ϕ at earlier time steps. Hence, the temporal discretization is always an extrapolation. For the presentation of the temporal discretization, eq. (5.26) is reformulated by denoting the discretization of the advective and diffusive fluxes by the operator $\mathcal{F}(\phi)$:

$$\int_V \frac{\partial\phi}{\partial t} dV = \mathcal{F}(\phi) \tag{5.32}$$

First, the time derivative can be assumed to be constant over the control volume

$$\int_V \frac{\partial\phi}{\partial t} dV \approx \frac{\partial\phi}{\partial t}\delta V, \tag{5.33}$$

leading to:

$$\frac{\partial\phi}{\partial t} = \frac{1}{\delta V}\left[\mathcal{F}(\phi)\right]. \tag{5.34}$$

In principal, one can distinguish between explicit and implicit schemes. An explicit scheme is of the following form,

$$\phi^{n+1} = \mathcal{F}(\phi^n, \phi^{n-1}, ...), \tag{5.35}$$

where $\phi^n = \phi(t^n)$. Explicit schemes use only old values of ϕ, whereas implicit schemes use also the current time step;

$$\phi^{n+1} = \mathcal{F}(\phi^{n+1}, \phi^n, \phi^{n-1}, ...). \tag{5.36}$$

Consequently, ϕ^{n+1} cannot be determined directly by an implicit scheme, but has to be computed by an iterative algorithm.

Explicit schemes have the disadvantage, that the time step is limited by the fact that information must have 'enough time' to travel from one mesh node to the neighboring during one time step. This reasoning leads to the Courant-Friedrich-Lewis limit (CFL) on the time-step, which for compressible flows reads,

$$CFL = \frac{|U| + a\Delta t}{\Delta x} < 1, \tag{5.37}$$

where U is the maximum convective velocity of the flow problem and a is the speed of sound. For implicit schemes there is formally no such limit, however for LES applications a Courant number below 1 is recommended in order to resolve the smallest eddies also temporally.

A simple implicit scheme, the so-called implicit Euler scheme, is defined by the backward difference,

$$\frac{\phi^{n+1} - \phi^n}{\Delta t} = \mathcal{F}(\phi^{n+1}). \tag{5.38}$$

This first-order scheme was used for all computations. The comparably low order is justified by the very small time steps resulting from the CFL limit.

5.4.2. *Solvers*

The discretization of the Navier-Stokes equation leads to a linear equation system for each time step. This equation system can in principle be solved for all variables simultaneously (coupled solver). However, for low velocities, the equations become almost incompressible and stiff. The pressure equation is not well posed for these conditions, resulting in slow convergence and long computation times.

For subsonic problems, it is therefore more useful to solve the equations successively by so-called uncoupled or segregated solvers, originally developed for the incompressible equations. The basic principle of these solvers is to solve the momentum equations resulting from an estimated pressure field, e.g. the pressure of the previous time step. The solution of the momentum equations does in general not fulfill the mass conservation equation. Thus, the velocities, densities and the pressure have to be corrected in order to fulfill the mass conservation equations. This is done by solving a Poisson equation in order to update the pressure. With this pressure, the velocities and densities are updated. Repeating this procedure until convergence delivers a solution that fulfills both the momentum and mass conservation. Throughout this thesis the Pressure Implicit with Splitting Operators (PISO) method is used for pressure coupling (for details see e.g. Ferziger & Peric (1996)). For the computations, the open source CFD solver OpenFoam[2] is used.

5.5. Evaluation of mixing quality

After a computation has been completed, the scalar concentration field is available. However, it is not obvious how to determine if the mixing is good or not. Perfect mixing would be achieved, if the concentration is the same everywhere in the region of interest for all times. Deviations from that perfect state occur in both space and time.

For stationary problems, one may define, a uniformity index (UI) as proposed by Fric (1995). The index is calculated from the time-averaged concentration in a

[2] www.openfoam.com

cross-section A of the geometry. It is defined as:

$$UI = 1 - \frac{\int_A |C_A - \overline{C_A}| dA}{[\int_A |C_A - \overline{C_A}| dA]_{ref}} \tag{5.39}$$

where C_A is the time averaged concentration in the considered cross-section and $\overline{C_A}$ is the average of C_A in the cross-section. The denominator is a reference value, which should correspond to the maximum value of the integral, i.e. completely separated species. UI gives a simple measure between 0 and 1 for the spatial uniformity of the mean concentration. A similar measure is the variance of segregation defined as

$$s^2 = \frac{1}{M-1} \sum_{i=1}^{M} (C_{A,i} - \overline{C_A})^2, \tag{5.40}$$

where M is the number of grid points in the cross-section (see Danckwerts (1952)). The intensity of segregation is obtained by normalization with the maximum value of the segregation,

$$I_s = \frac{s^2}{s^2_{max}}. \tag{5.41}$$

How the non-uniformity changes in time is, however, not included in these indicators. One possibility to assess the fluctuation intensity of the concentration over time is the RMS of the concentration, which gives a measure of the concentration fluctuations.

In order to assess the spatial non-uniformity for a pulsating flow, the uniformity index is redefined in a phase-averaged sense as

$$UI_{ph} = \frac{1}{N} \sum_{\phi_i} \left(1 - \frac{\int_A |C_{ph,A}(\phi_i) - \overline{C_{ph,A}}(\phi_i)| dA}{[\int_A |C_{ph,A}(\phi_i) - \overline{C_{ph,A}}(\phi_i)| dA]_{ref}} \right), \tag{5.42}$$

where ϕ_i denotes the phase angle, $C_{ph,A}$ is the phase-averaged concentration in the cross-section and $\overline{C_{ph,A}}$ is the mean of $C_{ph,A}$. N is the number of samples per period.

The evaluation of the mixing quality in the special case of engine flow demands the definition of different averages and RMS quantities. For the analysis of the mixture distribution among the cylinders and over the cylinder port cross-sections, the concentration and other flow variables are saved on surfaces close to the cylinder ports at least 100 times per cycle over 20 cycles. For the evaluation of this data, the following measures are defined:

The conventional cycle average over the cross-section and over time is given by,

$$c_{Cycle\ Average} = \frac{1}{NM} \sum_{i,j} c_{ij}, \tag{5.43}$$

where, the index i denotes the time sample and the index j denotes the cell count over the cross-section. N is the Number of samples and M the number of cells in the cross-section. u^n is the velocity normal to the considered cross-section and A is the cross-section area.

In order to evaluate the EGR content of the mixture entering the cylinders, the concentration is weighted by the mass flux into the cylinders, yielding

$$c_{Into\ Cylinder} = \frac{\iint c\rho u^n dAdt}{\iint \rho u^n dAdt} \approx \frac{\sum\limits_{i,j} c_{ij}\rho_{ij}u_{ij}^n}{\sum\limits_{i,j} \rho_{ij}u_{ij}^n}. \tag{5.44}$$

A measure for the mixing quality is the *spatial* Root Mean Square (RMS) of the concentration over the port cross-sections. Also the RMS can be weighted by the mass flux in order to exclude contributions from times where there is no flow through the port. The mean of the spatial RMS over a cross-section is computed as,

$$c_{rms\ Cycle\ Averaged} = \frac{1}{N}\sum_i \left(\sqrt{\frac{1}{(M-1)}\sum_j \left(c_{ij} - c_{i,mean}\right)^2} \right) \tag{5.45}$$

and the weighted RMS is defined as,

$$c_{rms\ Into\ Cylinder} = \frac{\sum\limits_i \sqrt{\frac{1}{(M-1)}\sum\limits_j \left[\rho_{ij}u_{ij}^n \left(c_{ij} - c_{i,mean}\right)\right]^2}}{\sum\limits_{i,j} \rho_{ij}u_{ij}^n}, \tag{5.46}$$

where $c_{i,mean}$ is the mean of the concentration over the cross-section at time i.

In order to quantify the variation in time of the EGR concentration the RMS of spatially averaged concentration is computed as

$$c_{rms\ time} = \left(\sqrt{\frac{1}{(N-1)}\sum_{i=VO}^{VC} \left(c_{i,mean} - c_{mean}\right)^2} \right). \tag{5.47}$$

Here, only the samples during the time the valves are open are considered, i.e. from the valve opening (VO) to the valve closure (VC).

5.6. Flow Decomposition methods

The flow decomposition methods POD and DMD are introduced shortly in this section. For more detailed descriptions see e.g. Chatterjee (2000) for POD and Rowley *et al.* (2009) for the DMD.

The principal idea of both methods is to decompose the field $u(x,t)$ into temporal components $a_i(t)$ and spatial modes $\Phi_i(x)$, such that

$$u(x,t) = \sum_i^l a_i(t)\Phi_i(x). \tag{5.48}$$

$u(x.t)$ can be any variable of interest both in the form of vector and scalar fields.

POD is aiming to find the modes that for any l give the optimal (in a least square sense) approximation of u(x,t), i.e.

$$\min_{\Phi_i} \left(u - \sum_{i}^{N} a_i \Phi_i \right)^2 , \quad \forall i, \tag{5.49}$$

while fulfilling the orthogonality of the modes, i.e.

$$\Phi_i^T \Phi_j = \delta_{ij}, \tag{5.50}$$

where δ_{ij} is the Kronecker delta.

For the determination of the POD modes, N snapshots of the data on M grid points are saved at equidistant times Δt and arranged in the snapshot matrix $\mathbf{U}$ as

$$\mathbf{U} = [u_1, u_2, \dots u_N], \tag{5.51}$$

where the index is the snapshot number.

In can be shown, that the optimization problem in eq. (5.49), can be expressed by the following eigenvalue problem for the covariance matrix $\mathbf{U}\mathbf{U}^T$ (see Liang *et al.* (2002)).

$$\left(\mathbf{U}\mathbf{U}^T \right) y = \lambda y. \tag{5.52}$$

However, the covariance matrix $\mathbf{U}\mathbf{U}^T$ is very large for LES applications. The so-called *snapshot POD* is a way to circumvent this problem. Using the Singular Value Decomposition (SVD) of $\mathbf{U}$, yields

$$\mathbf{U} = \mathbf{V}\mathbf{\Sigma}\mathbf{W}^T. \tag{5.53}$$

$\mathbf{V}$ and $\mathbf{W}$ are orthonormal matrices and contain the eigenvectors of $\mathbf{U}\mathbf{U}^T$ and $\mathbf{U}^T\mathbf{U}$, respectively. $\mathbf{U}\mathbf{U}^T$ and $\mathbf{U}^T\mathbf{U}$ share eigenvalues, which are contained in $\mathbf{\Sigma}$. Therefore, the POD modes Φ_i can be written as the columns of $\mathbf{V} = \mathbf{U}\mathbf{W}\mathbf{\Sigma}^{-1}$ and the time coefficients a_i are the rows in $\mathbf{\Sigma}\mathbf{V}^T$.

A similar method, that is more focused on the dynamical behavior is Dynamical Mode Decomposition (DMD). Consider a linear dynamical system in the form:

$$u(x, t + \Delta t) = \mathbf{A} u(x, t) \tag{5.54}$$

Also for the DMD, N snapshots of the quantity of interest u_i are saved at uni-distant times. The snapshot matrix is formed in the following way:

$$\mathbf{U}_1^n = [u_1, u_2, ..., u_n]. \tag{5.55}$$

In this slightly different notation the lower index denotes the first snapshot number and the upper the last snapshot number. Following eq. (5.54), we assume that a linear mapping $\mathbf{A}$ exists, such that

$$u_{i+1} = \mathbf{A} u_i \tag{5.56}$$

$$or \quad \mathbf{U}_2^n = \mathbf{A}\mathbf{U}_1^{n-1} \tag{5.57}$$

and that $\mathbf{A}$ is approximately constant during the time spanned by the snapshots. A contains the temporal information of the dynamical process. In principal we seek

therefore for the eigenvalues and eigenvectors of $\mathbf{A}$. This is, however, computationally expensive because $\mathbf{A}$ is large. If the number of snapshots is sufficient, $\mathbf{U}_1^N$ contains all the dynamic information of the process and the vectors u_i are linearly dependent. The last velocity vector can then be written as a linear expression of the previous ones as,

$$u_n = a_1 u_1 + a_2 u_2 + ... + a_{n-1} u_{n-1} + r, \tag{5.58}$$

where the a_i can be obtained by a least-square method and r is a residual that has to be minimized. Eq. (5.57) can then be rearranged in the following way:

$$\mathbf{A}\mathbf{U}_1^{n-1} = \mathbf{U}_2^n = \mathbf{U}_1^{n-1}\mathbf{S}, \tag{5.59}$$

where $\mathbf{S}$ is the companion matrix

$$\mathbf{S} = \begin{bmatrix} 0 & & & & a_1 \\ 1 & 0 & & & a_2 \\ & \ddots & \ddots & & \vdots \\ & & 1 & 0 & a_{n-2} \\ & & & 1 & a_{n-1} \end{bmatrix} \tag{5.60}$$

The eigenvalues of $\mathbf{S}$ represent an approximation of the eigenvalues of $\mathbf{A}$. However, in practical application the eigenvalues of a sparse matrix are not well-posed. Therefore, it is preferable to first perform a SVD of the snapshot matrix as $\mathbf{U_1^{n-1}} = \mathbf{V\Sigma W^T}$. A full companion matrix defined as $\tilde{\mathbf{S}} = \mathbf{V^T A V}$ is obtained using eq. (5.59) as

$$\tilde{\mathbf{S}} = \mathbf{V}^T\mathbf{A}\mathbf{V} = \mathbf{V}^T\mathbf{U}_2^n\mathbf{W}\mathbf{\Sigma}^{-1}. \tag{5.61}$$

The dynamic modes are then found by

$$\Phi_i = \mathbf{V}\mathbf{y}_i, \tag{5.62}$$

where $\mathbf{y}_i$ is the i-th eigenvector of $\tilde{\mathbf{S}}$. The associated frequency is given by

$$f_i = \frac{1}{2\pi}\arctan\left(\frac{Im(\lambda_i)}{Re(\lambda_i)}\right)/\Delta t, \tag{5.63}$$

where λ_i is the i-th eigenvector of $\tilde{\mathbf{S}}$. The physical quantity described by mode m, $u^m(t)$, can be obtained by reconstruction of the mode as

$$u^m = Re\left\{\Phi_m e^{-2\pi f t}\right\} = \tag{5.64}$$

$$Re\{\Phi_m\}\cos(2\pi f t) + Im\{\Phi_m\}\sin(2\pi f t) = \tag{5.65}$$

$$\sqrt{Re^2\{\Phi_m\} + Im^2\{\Phi_m\}}\left(\sin\left(2\pi f t + \arctan\frac{Re\{\Phi_m\}}{Im\{\Phi_m\}}\right)\right) \tag{5.66}$$

From this, one can see that the amplitude of each mode is described by the magnitude of the complex Φ_m.

The modes obtained by POD are the optimal orthogonal modes in the sense that they give the modes that contain the most possible energy. As a result of the SVD, the modes are automatically sorted by their energy content, i.e. the first mode is the most energetic, the second one is the second most energetic and so on. Thus, one can

obtain a reduced flow field by reconstruction from only a few of the first modes that gives a representation of the most energetic flow structures while being much easier to interpret as compared to the original turbulent flow field. DMD, on the other hand, decomposes the flow variables into modes containing certain frequencies independent of their energy content. In order to find the most significant modes, one has to sort the modes by their strength, using e.g. the L_2-norm. In principal it is also possible to reconstruct the field from the DMD modes. The strength of DMD lies, however, in the possibility to isolate and identify the 3-D shape of given frequencies and thereby providing insight into the dynamics at these frequencies. This is of advantage if one is looking for the behavior of modes with known frequency that might not be the most energetically dominant and thus be oblique in POD.

CHAPTER 6

Selected results and discussions

This section summarizes some of the most important results of the thesis research. First, a description of the (stationary) flow in two T-junction geometries and the observed flow modes under varying flow ratios between the main and the branch pipe. Moreover, the dependence of the mixing quality on the flow ratio is analyzed. Thereafter, the results from the stationary flow are compared to computations applying a pulsating inflow condition on the branch inlet.

Finally, LES is applied to simulate the transitional and turbulent flow in two realistic engine manifolds using boundary conditions from one-dimensional computation and/or experimental data. The mixing quality of the air/EGR mixture, that enters the cylinders is evaluated in terms of spatial and temporal variances. POD and DMD are applied in order to extract the dominant flow modes. On the basis of these findings, the observed non-uniform EGR distribution can be explained.

6.1. Flow and mixing in T-junctions

6.1.1. *Mean flow characteristics*

Two T-junction geometries are analyzed as a basis for the engine computations. The simplified geometries have the advantage of an easier meshing and data acquisition as compared to complex engine geometries. Another advantage is the possibility of comparison with experimental data in terms of velocity measurements, which is seldom available for complex engine geometries. Apart from that, the results of the simplified computations are easier to understand and allow for more detailed analyzes of the flow characteristics. The geometries are depicted in Fig. 6.1. The first geometry is a junction of two square ducts with an angle of $90°$, whereas the second one consists of two circular pipes with the same angle. The comparison of the two junctions is performed for a flow ratio of $R_f = \frac{\dot{m}_m}{\dot{m}_b} = 2$ between the main and the branch pipe, which is equivalent to a velocity ratio of 1 in both junctions. An accuracy study using different resolutions is carried out and the LES results are compared to experimental data in Paper 1. For sufficient resolution, the agreement of the simulation with experimental data is good in terms of velocity profiles and scalar distributions.

Fig. 6.2 shows the mean axial velocity in the center plane of both junctions. Past the junction there is a recirculation zone with negative mean velocities. One can see that the recirculation has different shapes depending on the configuration. For the circular junction, the recirculation is detached from the upper wall, because

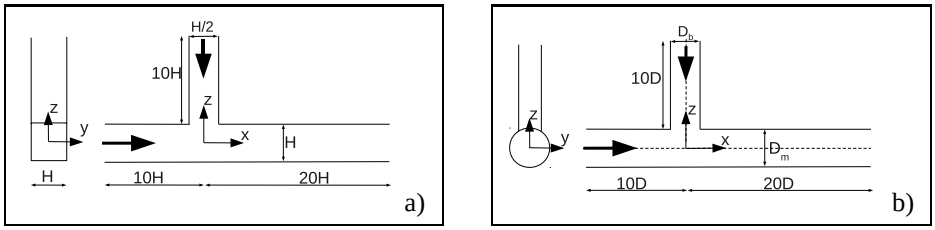

FIGURE 6.1. Computational domains; a) T-junction with square cross-sections, b) T-junction with circular cross-sections ($\frac{D_m}{D_b} = 1.4$)

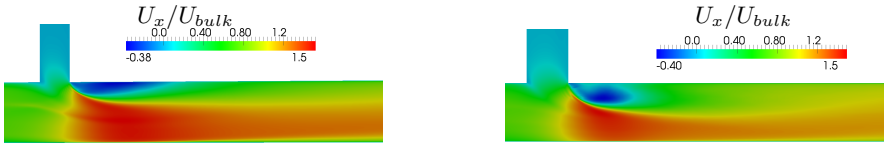

FIGURE 6.2. Mean axial velocity in the center plane for $R_f = 2$: a) Square T-junction, b) Circular T-junction

fluid is allowed to flow around the branch jet. In the square junction, this is not the case and the recirculation has a larger axial width. As a consequence the position of the shear layer is further away from the upper wall in the circular junction and the jet is entrained further into the main pipe. Below the recirculation, there is a strong shear layer, leading to high turbulence intensities. In Fig. 6.3, profiles of the turbulence intensity $I_{turb} = \sqrt{\frac{1}{3}u_{rms}^2 + v_{rms}^2 + w_{rms}^2}/U_{bulk}$ [1] are plotted at several axial positions over z. The peaks are located at the position of the shear layer and are up to 40% of the bulk velocity. For $x > 8D$ [2], the effect of the branch disturbance is hardly visible and the profiles are similar to fully developed pipe/duct flow.

The secondary structures are similar in both junction. Downstream of the junction, the flow curvature causes the formation of a Counter-rotating Vortex Pair (CVP). These vortices are similar to the ones found in bend pipes, the so-called Dean vortices (see e.g. Dean (1928)). They are caused by the centrifugal forces which are larger in the center of the pipe than in the outer regions close to the walls. Further downstream, these vortices are dissipated and a CVP rotating in the opposite direction is formed. Fig. 6.4 shows the mean axial vorticity and the in-plane vectors in some cross-sections past the junction together with a streamline originating from the branch pipe. One can see that the CVPs are counter-acting the direction of the streamline.

The downstream CVP is found to have a big impact on the mean scalar distribution over the pipe cross-sections.

[1] U_{bulk} denotes the bulk velocity in the main pipe downstream of the junction.
[2] unless stated otherwise $D = D_m$

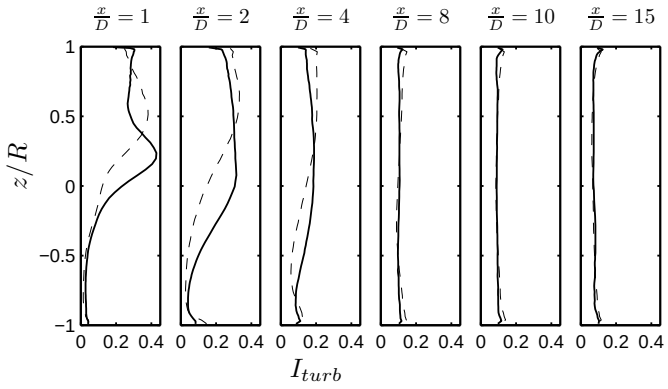

FIGURE 6.3. Turbulence intensity over some cross-sections for the circular pipe junction (solid line) and the square duct junction (dashed line), $R = D/2$, $R = H/2$, respectively

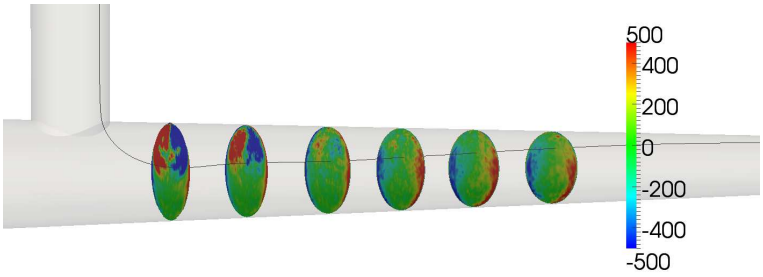

FIGURE 6.4. Distribution of the mean streamwise vorticity component in the main pipe downstream of the junction; red color - indication of clockwise rotation; blue color - counter-clockwise rotation

Fig. 6.5 shows the mean in-plane vectors at $x = 5D$ and the mean concentration computed by LES and by RANS-k-ϵ. The RANS approach does not predict the switch of direction of the CVP observed in the LES. The result is a qualitatively different mean scalar distribution. The reason for this difference is found in the dissipative behavior of the $k - \epsilon$-model. The consequence is that the upstream CVP is not dissipated properly, which does not allow for the formation of the downstream CVP.

When changing the flow ratio between the main and the branch flow, different flow patterns can be observed (see Igarashi *et al.* (2002)). For high flow ratios, the jet stays attached to the upper wall, which is referred to as *wall jet*. At intermediate flow ratios the jet is detached from the upper wall without impinging on the opposite wall. This case is called *deflecting jet*. At the limit of small flow ratios, the jet is impinging on the opposite wall of the main pipe. This pattern is denoted by *impinging*

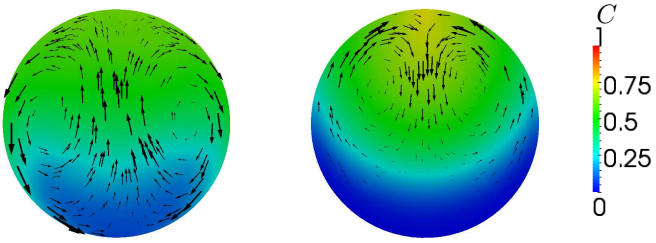

FIGURE 6.5. Mean in-plane vectors and scalar concentration at $x = 5D$ for $R_f = 2$ computed by LES (left) and RANS-k-ϵ (right)

jet. Fig. 6.6 shows the mean axial velocity profiles and the turbulence intensities at several downstream positions for different flow ratios normalized by the bulk flow velocity downstream of the junction. The radial dimensions of the recirculation are increasing with decreasing flow ratio. Also the strength of the shear layer and the turbulence intensity is increasing with decreasing flow ratio. The impingement is causing additional turbulence production resulting in turbulence intensities of up to 60% of the of the bulk velocity.

The increase in turbulence intensity at small flow ratios is enhancing the mixing quality. Fig. 6.7 shows the uniformity index computed by eq. (5.39) and the maximum of the scalar RMS in cross-sections downstream of the junction. The spatial uniformity is decreasing with increasing flow ratio, whereas the largest intensity of the scalar fluctuations is found for $R_f = 2$. The lowest scalar fluctuations are observed at the impinging cases, indicating the best mixing quality.

For the application in engine design this means that the mixing quality can be improved by making sure that the jet impinges on the opposite wall, i.e. decreasing the branch pipe diameter for a constant EGR rate. The pressure drop over the junction is then, however, increasing.

6.1.2. *Flow modes (instabilities)*

The flow modes observed in the T-junctions can be summarized as follows.

The strong shear layer observed along the z-direction causes a Kelvin-Helmholtz instability inside the shear layer. This flow mode is observed in both geometries. The frequency of this mechanism scales with the shear layer momentum thickness. In agreement with linear stability analysis (see e.g. Ho & Huerre (1984)), the normalized frequency based on the shear layer momentum thickness Θ, $f^*_\Theta = \frac{f\Theta}{U_{bulk}}$, of this mode is about 0.03 (see Fig. 6.8a). The spatial extent of this mechanism is, however, limited to a small region in the shear layer. Further downstream, the Kelvin-Helmholtz mechanism is less dominant. In the circular pipe junction, a vortex shedding past the branch jet is dominating the flow and the scalar mixing. The normalized frequency based on the branch diameter and the bulk flow velocity, $f^*_{D_b} = \frac{fD_b}{U_{bulk}}$, is dependent

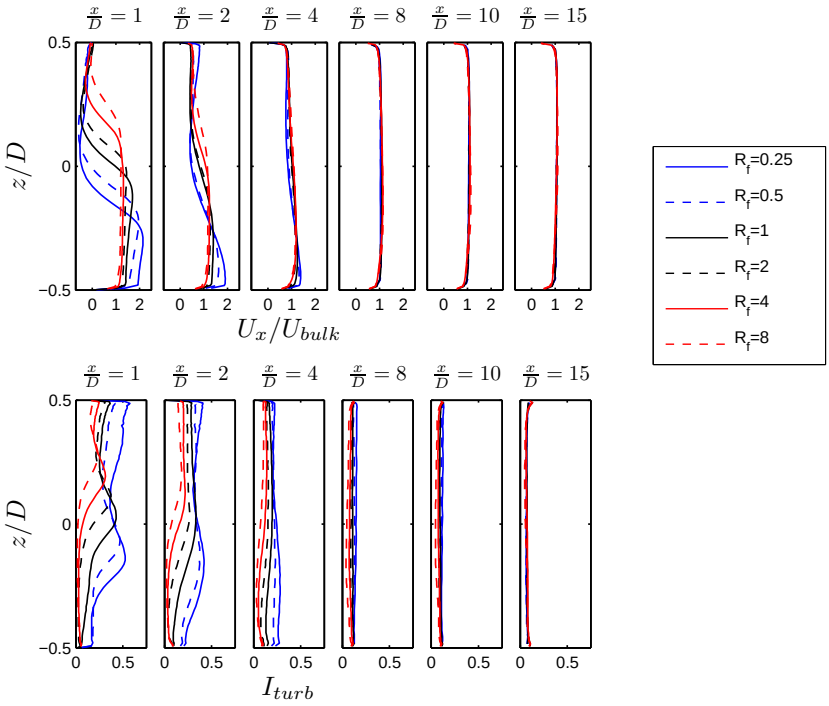

FIGURE 6.6. Profiles of mean axial velocity (top) and turbulence intensity (bottom) for different flow ratios

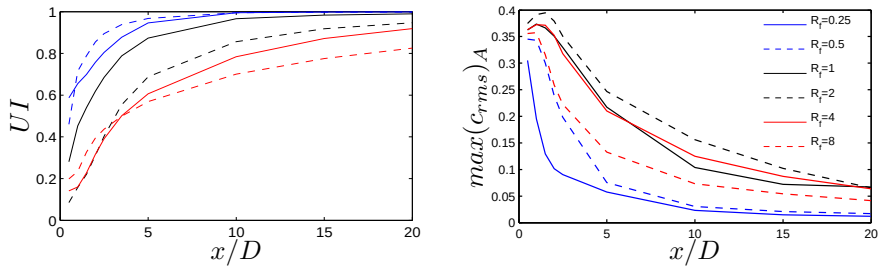

FIGURE 6.7. Mixing quality indicators: Left: Uniformity Index for different flow ratios, Right: Maximum of c_{rms} over cross-sections

on the flow ratio (see Fig. 6.8b). Moreover, it is found to be significantly higher than the values of 0.2 reported in a previous study of a T-junction with a diameter ratio

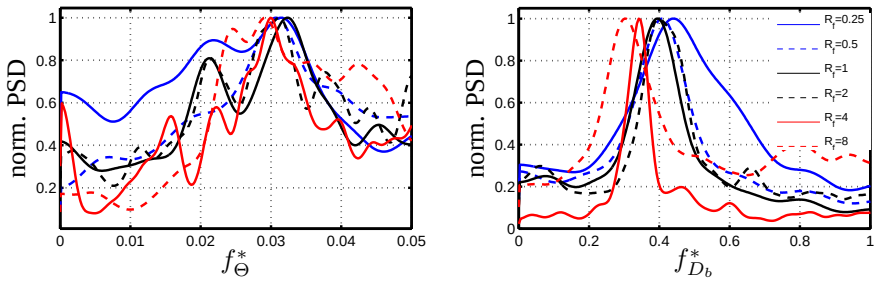

FIGURE 6.8. Power spectra normalized with the maximum value: Left: PSD of u_z at points inside the shear layer with $x = 1.5D$ over f^*_Θ, Right: PSD of u_y at $x = 3D$, $y = 0$, $z = 0$

FIGURE 6.9. Iso-surfaces of the y-component of the strongest DMD mode at a frequency of $f^*_{D_b} = 0.4$ for $R_f = 2$

between the main and the branch pipe of 3 (see Kamide *et al.* (2009)) and in jet-in-crossflow studies (see e.g. Rowley *et al.* (2009)). This discrepancy is attributed to the confinement in form of the pipe walls, which decreases the space available for the vortex shedding. The walls are closer to the jet, when the diameter ratio is small. In the present case the diameter ratio is 1.4, i.e. the confinement is likely to have a larger influence on the flow mode than with a diameter ratio of 3. Also the dependency of the vortex shedding frequency can be explained following this reasoning. As the flow ratio decreases, the recirculation zone increases and gives the jet less space to develop, which increases the shedding frequency.

The vortex shedding is also studied using DMD. For the DMD, 600 snapshots of the instantaneous velocity field were used with a sampling frequency of 5 kHz, which corresponds to $f^*_D = 9.3$. Fig. 6.9 shows positive and negative iso-surfaces of the DMD mode corresponding to the peak frequency ($f^*_{D_b} = 0.4$) of the energy spectrum in Fig. 6.8a for $R_f = 2$. One can clearly see the alternating structures. The structures are tilted over the pipe because of the higher velocities in the center of the pipe.

6.1.3. *Pulsating inflow conditions*

In order to mimic pulsating EGR flow a strong sinus-shaped fluctuating mass flow is prescribed on the branch inlet, as

$$\dot{m}_b(t) = \frac{1}{2}\dot{m}_m \cdot [\sin(2\pi f t) + 1], \tag{6.1}$$

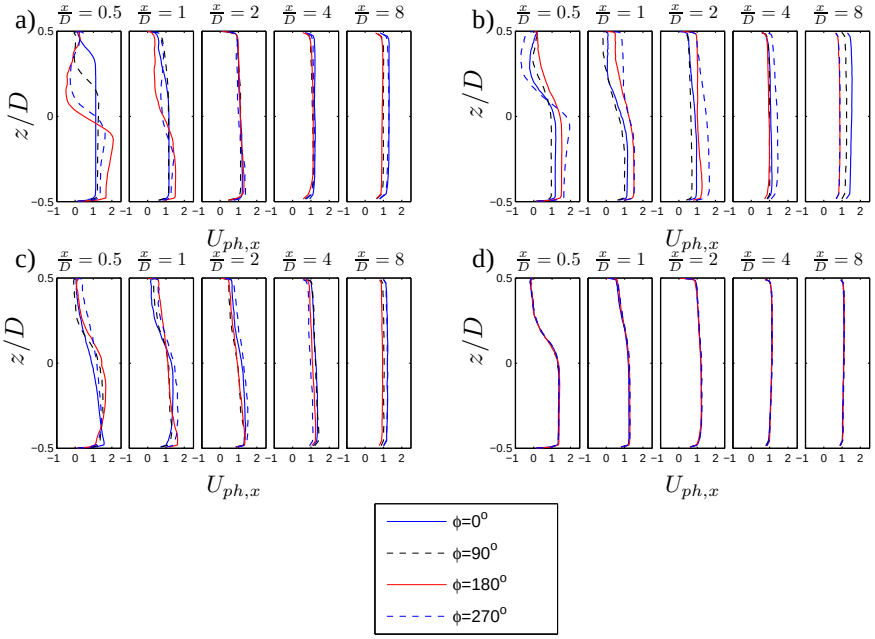

FIGURE 6.10. Phase averaged velocity profiles for a) $St = 0.056$ ($f = 30$ Hz), b) $St = 0.224$ ($f = 120$ Hz), c) $St = 0.56$ ($f = 300$ Hz) and d) $St = 1.12$ ($f = 600$ Hz)

where $\dot{m}_m$ is the constant mass flow at the main pipe inlet. The frequency f is varied between 30 Hz and 600 Hz. The frequencies are normalized using the Strouhal number $St = \frac{fD_m}{U_{bulk}}$. The mean flow ratio is 2. Fig. 6.10 and 6.11 show the phase-averaged axial velocity and scalar profiles over z at several axial positions for four phase instances $\phi = 0^o, 90^o, 180^o$ and 270^o. Comparing the data obtained for different pulsating frequencies, it is obvious that the shape and the dynamics of the velocity are dependent on the pulsation frequency. For $St = 0.056$ and $St = 0.224$, the recirculation bubble cannot be observed during the whole cycle, but only at the phase angles around the maximum bulk velocity. With increasing frequency, the pulsations have less influence on the flow in the main pipe, i.e. the flow in the main pipe cannot adjust to the fast pulsations. For $St = 1.12$, the velocity profiles are almost constant over the period itself. For $St = 0.56$, back flow into the branch pipe occurs at some phase angles, which leads to higher turbulence intensity causing flatter velocity profiles.

The mixing quality is evaluated using the phase-averaged uniformity index UI_{ph} (see eq. (5.42)). Fig. 6.12 shows UI_{ph} over x for the pulsating cases. As a reference also UI for the stationary case with $R_f = 2$ is included. Compared to the stationary

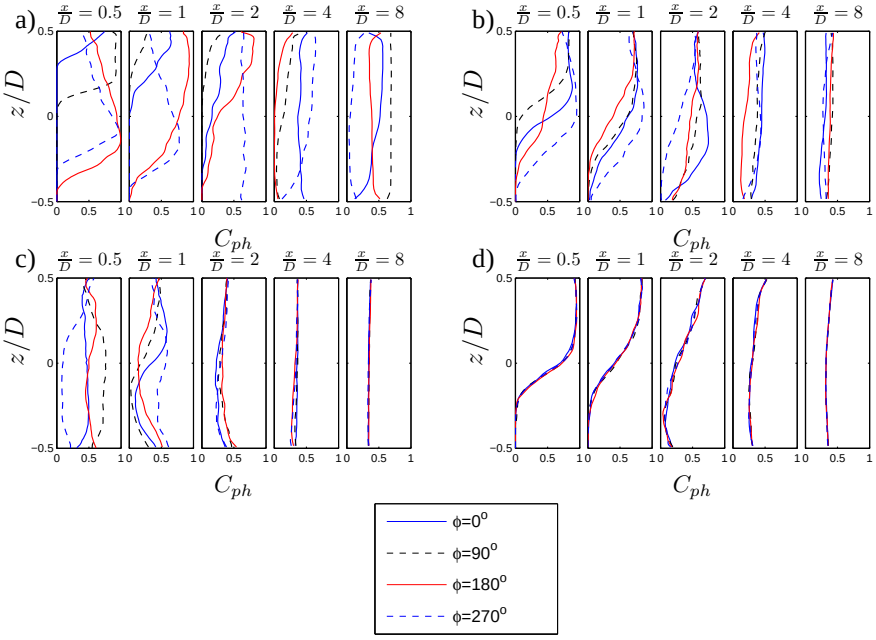

FIGURE 6.11. Phase-averaged scalar profiles for a) $St = 0.056$ ($f = 30$ Hz), b) $St = 0.224$ ($f = 120$ Hz), c) $St = 0.56$ ($f = 300$ Hz) and d) $St = 1.12$ ($f = 600$ Hz)

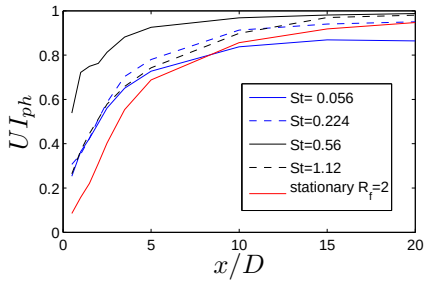

FIGURE 6.12. a) UI_{ph} for different pulsation frequencies

case, the uniformity is higher up to $x \approx 8D$ for all frequencies. For $St = 0.056$ and $x > 8D$ the phase-averaged non-uniformity is higher. Thus, the mixing quality is not necessarily increased by pulsating flow. For $St = 0.56$, the uniformity is overall higher due to the occurrence of back-flow.

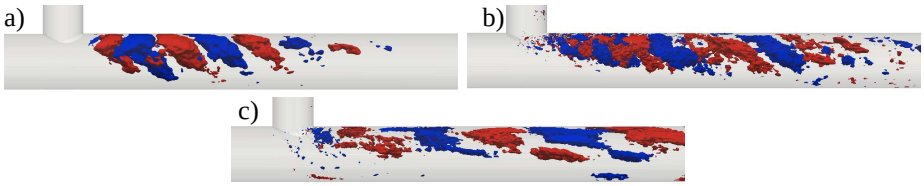

FIGURE 6.13. Positive (red) and negative (blue) iso-surfaces of the DMD modes of u_y, a) $St = 0.056$ ($f = 30\,\text{Hz}$), b) $St = 0.224$ ($f = 120\,\text{Hz}$), c) $St = 0.56$ ($f = 300\,\text{Hz}$)

6.1.4. *Flow modes in pulsating flow*

In strongly pulsating flow, it is obvious that the most dominant flow modes are the pulsations themselves. However, other modes such as the vortex shedding mechanism can still coexist. It is however difficult to identify such a behavior from the flow field alone. Flow decomposition methods such as POD and DMD have a potential to separate the flow mechanisms. Particularly DMD is useful in this context as it makes it possible to visualize the modes at different frequencies. With DMD, the vortex shedding phenomena could be identified also for the pulsating cases. Fig. 6.13 shows the mode corresponding to the shedding frequency for the pulsation frequencies $St = 0.056$, $St = 0.224$ and $St = 0.56$. The shedding frequency is varying with the pulsations, which leads to different wave lengths of the oscillations.

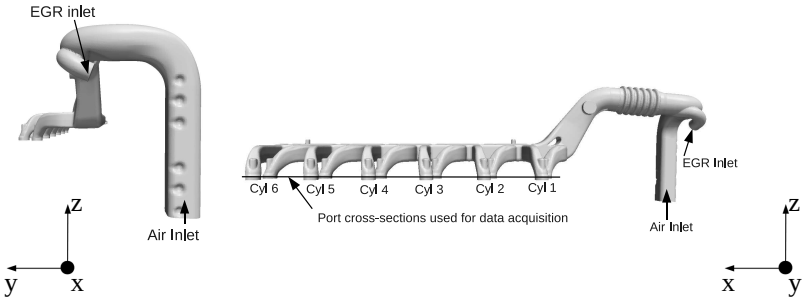

FIGURE 6.14. Inlet manifold from a Scania six cylinder Diesel engine including the definition of cross-sections used in the result section

6.2. EGR mixing in the SCANIA manifold

The flow and the EGR mixing are investigated in a manifold of a six-cylinder Diesel engine. This section starts with a description of the boundary conditions used in this study. Thereafter, the flow field and the EGR concentration are investigated using POD and DMD. Furthermore, the results are analyzed in terms of EGR non-uniformity and sensitivity to changes in the boundary conditions. Experimental data, obtained within the Competence Center of Gas Exchange (CCGEx), is used for validation purposes.

6.2.1. *Boundary conditions*

To obtain the boundary conditions for the 3D-simulation, a combination of experiments and 1D-simulation data is used. As inflow boundary conditions, measured pressure traces from the air path and the EGR path of the engine are used. The outflow boundary condition, i.e. the mass flow, was computed from a calibrated 1D-simulation with the commercial software GT-Power®. The considered load case is 1200 rpm, the EGR rate is approximately 30% EGR.

Fig. 6.15 shows the inlet and outlet conditions for one engine cycle. The resulting flow is highly pulsating with velocities at the EGR inlet ranging from -100 to 100 m/s. The Reynolds number based on the mean flow velocity and the largest diameter is about 500,000.

6.2.2. *Flow characteristics by POD and DMD*

POD and DMD is applied both to the velocity field and the concentration field. For both the POD and the DMD, 1200 snapshots are used with a sampling frequency of $f = 600$ Hz, i.e. 60 snapshots per engine cycle. The snapshot space spans 2 seconds of physical time or 20 engine cycles.

6.2.2a. *POD.* As a consequence of the optimality, POD does not necessarily separate the flow into its frequency content. Therefore, one mode can in general contain several

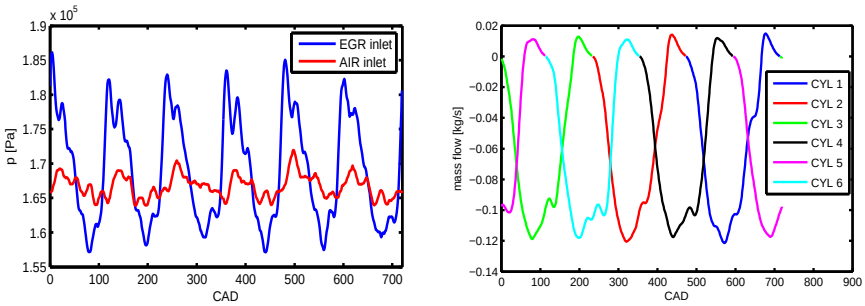

FIGURE 6.15. Boundary conditions; Left: pressure from on-engine measurements, Right: Mass flow to cylinders from one-dimensional simulations

frequencies and several physical phenomena. The temporal behavior of a mode is described by the coefficients $a_i(t)$. Fig. 6.16 shows the time coefficients of the first three POD modes and their frequency spectra for the velocity and the concentration.

Mode 0 of the velocity contains not only the mean field, but also pulsations at 30 Hz and 60 Hz. All other modes contain only pulsations around the mean field, which also have frequencies of 30 Hz and 60 Hz. In mode 2, the 30 Hz and 60 Hz frequencies are lower in amplitude and another pulsation at 10 Hz becomes more important.

The occurrence of these frequencies can be explained by the engine pulsations. 10 Hz corresponds to the valve opening frequency for each cylinder and 60 Hz is the firing frequency and the pulsation frequency of the EGR pulses. The somewhat surprisingly dominant frequency of 30 Hz can be explained by pressure pulses originating from the closure of the cylinder valves. These pressure pulses travel upstream and interact with the EGR pulses.

The time coefficients of mode 0 of the concentration contains almost only the mean concentration distribution. The next modes contain only the 30 Hz and the 60 Hz frequencies, the 10 Hz cannot be observed. This is due to the fact that the concentration field is dominated by the EGR pulses. Fig. 6.17 shows a comparison of the instantaneous concentration at Crank Angle Degree (CAD)=580 and the reconstructed concentration at the same CAD from the first 4 modes. At CAD 580, the first cylinder valve is open. One can clearly see how the POD captures the EGR pulses and filters out the turbulent fluctuations. This facilitates the interpretation of the results and shows that the pulsations are the reason for the observed maldistribution.

6.2.2b. *DMD.* DMD is used to extract the spatial structures at certain frequencies. Furthermore, DMD allows for ordering the modes at different frequencies by their L_2-norm. This gives a basis for weighting them according to their relevance on the flow field. Fig. 6.18 shows the L_2-norm of the DMD modes over the frequency for the velocity and the concentration field. In the velocity field, the strongest mode corresponds to the mean field, i.e. it has a frequency of 0 Hz. The second and third

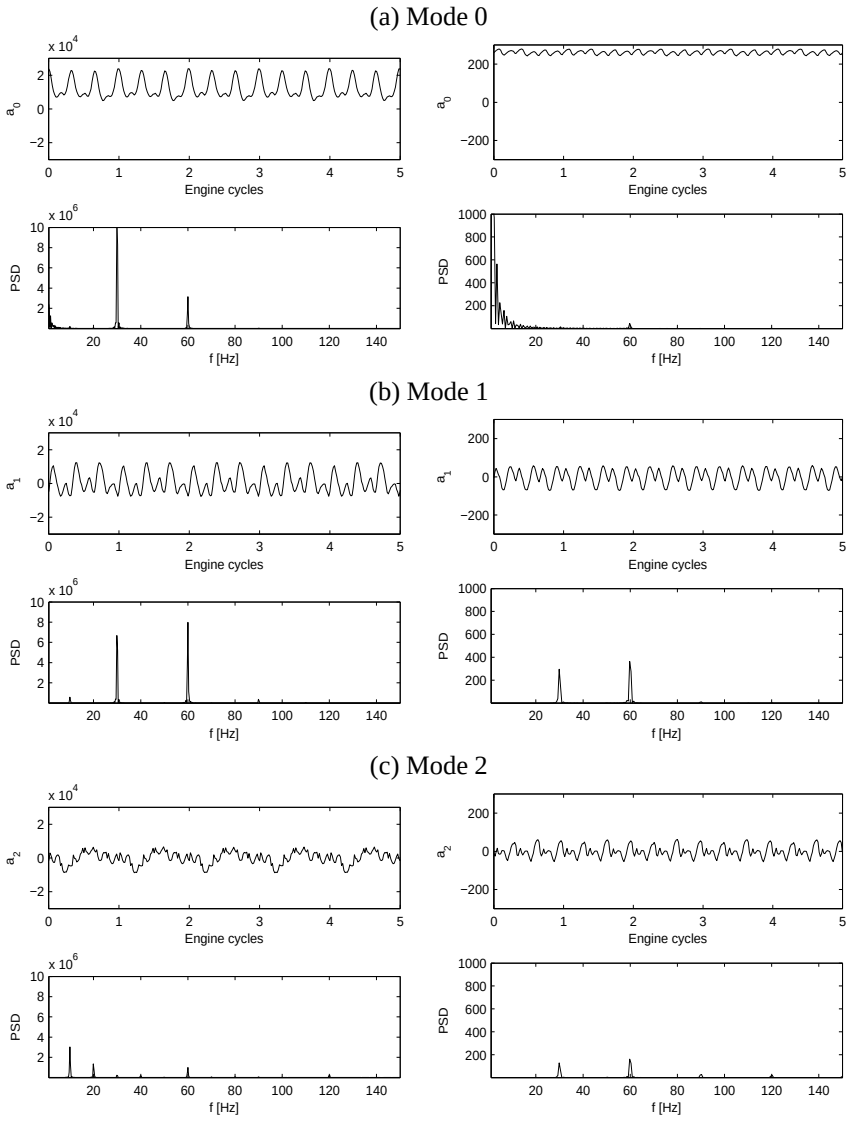

FIGURE 6.16. Time coefficients of the first 3 POD modes over five engine cycles and their frequency spectra computed for the velocity field (left column) and the scalar field (right column)

strongest modes are located at 30 Hz and at 60 Hz. Other peaks are found at 10 Hz (the valve opening frequency) and overtones of the 30 Hz, i.e. 90 Hz and 120 Hz. This is in agreement with the POD results. The spectrum of the DMD modes for

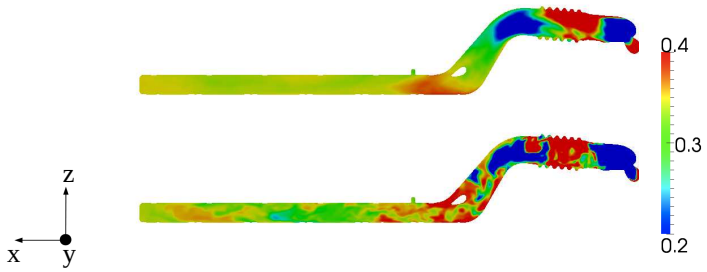

FIGURE 6.17. Concentration field in a xz-plane at CAD=580; top: reconstructed form the first 4 POD modes, bottom: instantaneous

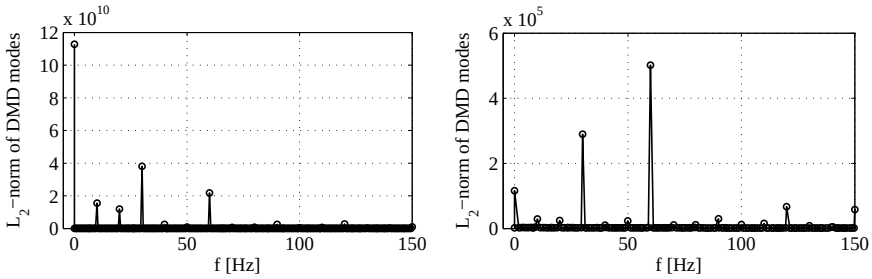

FIGURE 6.18. L_2-norm of the DMD modes. Left: Velocity, right: concentration

the concentration shows two dominant frequencies at 60 Hz and 30 Hz. The mean concentration (f=0 Hz) is smaller than these fluctuations. The reason for this is that the concentration is bounded between 0 and 1, i.e. the concentration fluctuation are relatively high compared to the mean concentration.

Fig. 6.19 shows iso-surfaces of the amplitude of the three largest DMD modes of the velocity field, at 30Hz, 60Hz and 10 Hz. The mode at 60 Hz is attributed to the EGR pulsations. The mode at 30 Hz is not directly seen in the EGR pipe, but is developing in the main pipe. As a result, the flow between the EGR inlet and the first cylinder is governed by a superposition of these two frequencies. The 10 Hz-frequency is attributed to the cylinder valve motion, which governs the flow close to the cylinder ports. These results show that the flow is dominantly governed by the engine pulsations and the interaction between them.

6.2.3. *Evaluation of mixing quality*

The results of the base-line case are evaluated using eq. (5.43) and eq. (5.44). Fig. 6.20 shows the EGR distribution normalized by the overall mean EGR rate, i.e. a value of 1 corresponds to *perfectly mixed*. The bars in Fig. 6.20 indicate the measures of the spatial non-uniformities defined by eq. (5.45) and eq. (5.46). The experimental data originates from CO_2 measurements over the whole cycle and can therefore only

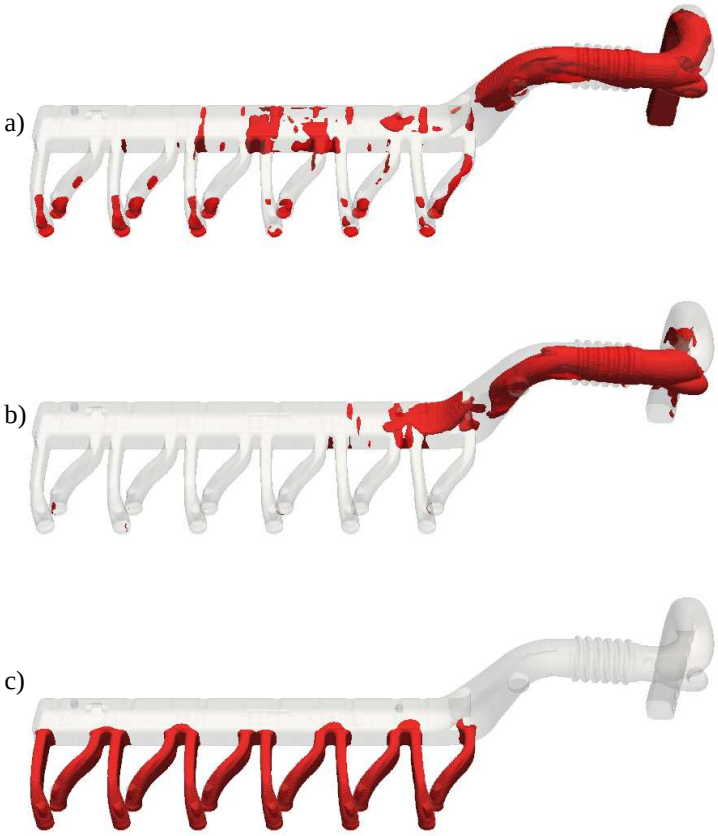

FIGURE 6.19. Iso-surfaces of the amplitude of the velocity DMD modes, computed as $\sqrt{Re^2\{\Phi_m\} + Im^2\{\Phi_m\}}$, at a) 30 Hz, b) 60 Hz and c) 10 Hz

be compared to the cycle-averaged concentration. The agreement with the experiment is good in terms of the cycle-averaged concentration. There are significant deviations from a perfect mixing both in terms of cylinder-to-cylinder variation (up to 6%) and over the port cross-sections (up to 20%). The difference between the cycle-average $c_{Cycle\ Average}$ and the weigthed $c_{Into\ Cylinder}$ is up to 6% at cylinder 1. This implies that the cycle-average might give misleading results, which is a possible weakness of the experimental method. Fig. 6.21 compares the spatial RMS $c_{rms\ Into\ Cylinder}$ to the temporal RMS $c_{rms\ time}$ computed by eq. (5.47). The deviation from the mean is in the same order both in space and time except of the cylinder 5 and 6 where the RMS in time is much higher than the spatial RMS.

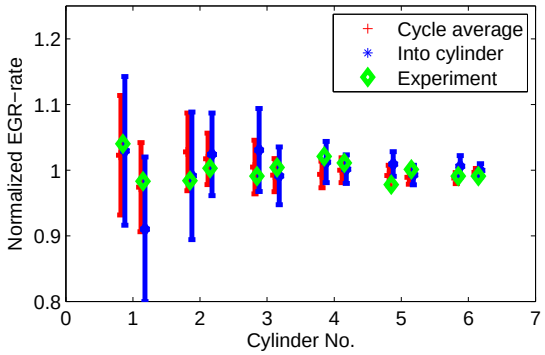

FIGURE 6.20. Different averages of cylinder-to-cylinder EGR distribution according to eqs. (5.43) and (5.44). Bars indicate the spatial RMS of the concentration over the outlet cross-sections computed by eqs. (5.45) and (5.46).

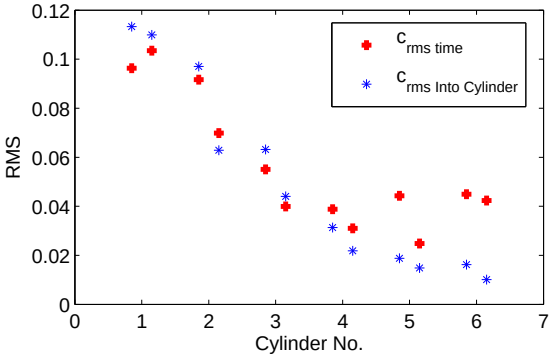

FIGURE 6.21. Spatial vs. temporal non-uniformity at the cylinder ports

In order to assess the sensitivity to uncertainties in the boundary conditions, several changes are applied to the base-line case. The mass flow is specified as simplified triangular functions and the amplitude and temperature of the EGR pulses are changed. The EGR pulse amplitude have the largest impact on the EGR distribution. The EGR temperature and the outlet conditions have less impact. Fig. 6.22 shows the results in terms of EGR concentration into the cylinders for different EGR pressure pulse amplitudes. With the higher amplitude, larger cylinder-to-cylinder variation is observed at the most upstream cylinders. Also the non-uniformity over the port cross-sections is larger for the higher pressure amplitude. When lowering the pressure amplitude, the results are similar to the base-line case. However, at the most downstream cylinder ports, higher non-uniformity is observed. In other words, a clear trend cannot be

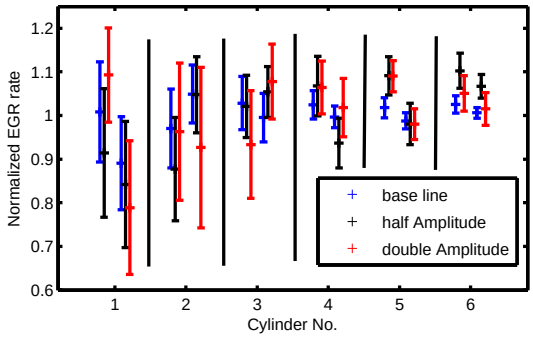

FIGURE 6.22. EGR distribution into the cylinders $c_{Into\ Cylinder}$ according to eq. (5.44) for different EGR pressure amplitudes. Bars indicate the spatial RMS of the concentration over the outlet cross-sections, $c_{rms\ Into}$ computed by eq. (5.46)

seen. This implies that higher EGR pulse amplitudes introduce larger non-uniformity, but also higher turbulence intensity, whereas the lower amplitudes introduce smaller non-uniformity but also lower capability of the flow to attain a fast mixing.

6.3. Comparison to a symmetric Volvo inlet manifold

Qualitative comparisons to another manifold taken from a Volvo four cylinder Diesel engine (see Fig. 6.23) are also performed. In this geometry the main air pipe is symmetric with respect to the cylinder intakes. The EGR pipe is connected to the main pipe through a junction. Below the EGR inlet, there is a so-called 'EGR-hat', a small metal sheet, which leads to the impingement of the EGR jet. This is supposed to give better mixing qualities similarly to what has been observed in the T-junction case. The boundary conditions for the Volvo case are taken from one-dimensional computation using the mass flow at the outlets and the pressure at the inlets over one engine cycle. Also in this case, the cylinder valves are not included in the domain.

Fig. 6.24 shows the EGR distribution for the Volvo case. Experimental data was provided by Volvo. The agreement between the experiments and the LES is good. Compared to the Scania case, the non-uniformity between the cylinders is larger with up to 10%. Over the cross-sections, the non-uniformity is much smaller (up to 5%) as compared to the first cylinder ports of the Scania manifold. The non-uniformity between the cylinders is caused by the position of the cylinder ports with respect to the main pipe and the skewed flow caused by the upstream pipe bends. This can be seen in Fig. 6.25, showing the x-component of the mean velocity and the mean EGR concentration in a cut through the xy-plane. Additionally, the in-plane velocity vectors in a cross-section downstream of the EGR inlet is plotted in Fig. 6.26. Downstream of the EGR inlet, the flow is tilted to the right hand side transporting more EGR to cylinder 3 & 4 than to cylinder 1 & 2.

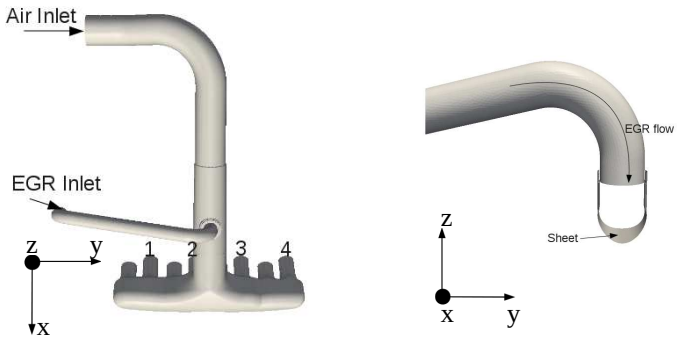

FIGURE 6.23. Left: Inlet manifold of a Volvo four cylinder Diesel engine (only one port per cylinder is open), right: detail of the EGR inlet pipe including the 'EGR hat'

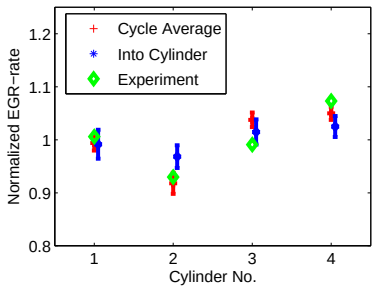

FIGURE 6.24. EGR distribution evaluated according to eqs. (5.43) and (5.44). The bars indicate the spatial RMS computed by eqs. (5.45) and (5.46)

In this sense, the mechanisms causing the cylinder-to-cylinder non-uniformity is different between the two geometries. Common for both geometries is the good agreement between the LES and the experimental data. This implies that the LES tool is suited for the computation and optimization of EGR distribution also in an industrial context.

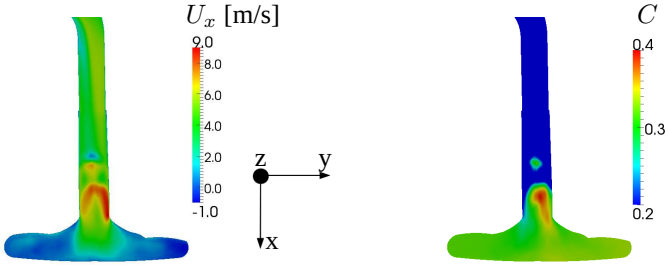

FIGURE 6.25. x-component of mean velocity (left) and mean EGR distribution (right)

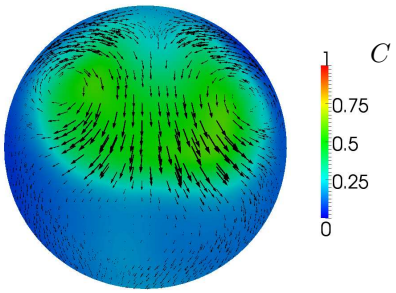

FIGURE 6.26. Mean in-plane velocity vectors downstream of the EGR Inlet, background color: mean EGR concentration

CHAPTER 7

Conclusions and future research perspectives

The problem of non-uniform EGR distribution in IC engines was investigated by LES. As a basis for that, computations were performed on two T-junction geometries with different cross-section shapes. These cases were used for the validation of the computational method together with a detailed analysis of the mixing processes under stationary and pulsating flow conditions. A grid sensitivity study was performed in order to ensure the accuracy of the numerical solution. The comparison to experimental data showed good agreement in terms of velocity and concentration profiles, whereby the accuracy of the modeling has been verified. RANS computations were performed in order to assess the differences and shortcomings of the RANS approach. Comparing RANS and LES results, qualitatively different secondary structures were found leading to different mean scalar distributions. It is concluded that RANS cannot accurately predict scalar distributions even in rather simple flow configurations. Two flow modes were found by spectral analysis of pointwise data and by DMD of volume data. Kelvin-Helmholtz vortices which are formed in both junctions due to the strong shear layer, located below the recirculation bubble past the inflow branch. In the configuration with circular cross-sections another flow mode is present. Past the branch jet, 'von-Karman' vortices are shed similarly to the well-known vortex shedding in the flow past a cylinder. This mode contains much more energy than the Kelvin-Helmholtz vortices and occupies a larger region downstream of the junction.

Varying the mass flow ratio between the main pipe and the branch pipe of the junction showed that the impingement of the branch jet on the opposite wall leads to higher turbulence production and thus higher mixing quality. However, the larger turbulence intensities and the larger recirculation bubble cause a larger pressure drop over pipe. The frequency of the vortex shedding was found to be dependent on the flow ratio and significantly higher than reported in previous studies on junctions with higher diameter ratio. It was concluded that the constriction of the pipe walls, which is closer to the jet when the diameter ratio is closer to 1, increases the vortex shedding frequency.

Pulsating boundary conditions with different frequencies were applied to the branch inlet in order to mimic the engine pulsations. Phase-averaged velocity profiles were presented showing that the flow is not quasi-stationary throughout the whole pulsation period. The recirculation zone is only visible during the phase of maximum flow. With increasing frequency, the flow in the main pipe is less affected by the pulsations, since

it does not adjust fast enough to the pulsations. In terms of phase-averaged spatial uniformity over pipe cross-sections, the pulsations do not necessarily enhance the mixing quality, since the pulsations introduce non-uniform scalar distributions over the pipe. DMD was applied to identify the vortex shedding mechanism also in the pulsating cases. The frequency of this flow mode is, however, changed by the pulsations.

The LES methodology was then used to compute the EGR mixing process in the inlet manifold of a six cylinder Scania engine. The flow was analyzed using advanced flow decomposition methods. With help of these techniques it was possible to extract the dominant flow structures from the large datasets of instantaneous velocities and concentrations. It was found that the flow is dominated by the pulsations originating from the recirculation of exhausts and the opening and closure of the cylinder valves. The EGR pulses govern the distribution of exhaust inside the manifold and are the primary reason for the maldistribution. The maldistribution over the cylinders and the temporal and spatial non-uniformity over the cylinder ports were quantified on the basis of the LES. Comparison with experimental data showed good agreement in terms of cycle averaged concentration. The amount of EGR actually entering the cylinders was, however, found to differ significantly from the cycle averaged concentration at some cylinder ports. Comparison to URANS computations showed that URANS predicts generally more uniform distributions, i.e. it over-predicts the non-uniformity. A sensitivity study with respect to changes of the boundary conditions, showed that the inlet boundary conditions, i.e. the amplitude of the EGR pressure pulses, are the most important boundary condition. The temperature of the EGR and the outlet conditions have less impact on the concentration distribution.

Finally, a second engine geometry was considered with very different flow characteristics due to a symmetric EGR supply relative to the cylinder valves. Also in this case, a good agreement was found between LES and experiments. Compared to the Scania manifold, the maldistribution is higher in terms of cylinder-to-cylinder distribution, but lower in terms of the distribution over the cross-sections. This was explained by the short distance between the EGR inlet and the outlets and the impact of the upstream pipe bends.

In summary, LES was found to be a suitable method for accurate predictions of EGR mixing in IC engines. Obviously, LES require adequate spatial and temporal resolutions and thereby require larger computational resources. However, with the computer resources available today LES should be an important tool also for industrial users.Key challenges are the prescription of accurate boundary conditions, particularly on the inlets to the domain. On the basis of these computations, it is possible to gain understanding of the governing flow mechanism and the reasons for observed maldistribution. This is particularly true when LES data is analyzed in conjunction with flow decomposition methods, such as POD and DMD. Moreover, on the grounds of LES data, it is possible to obtain information about the EGR flow that is hard to measure experimentally. Thus, LES is a powerful tool for the prediction and improvement of EGR distribution in inlet manifolds.

Based on the findings of this thesis, one might propose different designs for improved EGR distribution. As can be concluded from the T-junction computations, the diameter ratio between the EGR pipe and the main pipe is a way to control the entrainment of the exhausts into the air flow. Larger diameter ratios will, however, lead to higher pressure losses. Future research could therefore investigate the mixing quality and pressure loss when varying the diameter ratio both under stationary and pulsating flow conditions. In cases, where the EGR pulses are responsible for the maldistribution, one could propose to split up the EGR pipe into two or more and inject the EGR at different positions of the main pipe. This could lower the impact of the pulsations, but possibly also increase the pressure loss.

CHAPTER 8

Papers and Authors' Contributions

Paper 1

Turbulent flow mechanisms in mixing T-junctions by Large Eddy Simulations
A. Sakowitz (AS), M. Mihaescu (MM) & L. Fuchs (LF), 2012, submitted to *International Journal of Heat and Fluid Flow*

This paper deals with the flow computed by LES in two T-junction geometries with a flow ratio of $R_f = 2$ between the main pipe and the branch pipe. A grid sensitivity analysis of the LES data is performed and the results are compared to experimental data provided by Vattenfall. The discrepancies occurring due to the different geometries are analyzed. Moreover, the flow is analyzed in terms of secondary structures and flow modes. The computations and the data analysis were performed by AS under supervision of MM and guidance of LF. The paper writing was performed by AS with help and comments of MM and LF. Parts of these results have been presented and published in:

LES of the turbulent mixing process in a T-junction with stationary and pulsating inflow conditions
A. Sakowitz and L.Fuchs, 2011, 10th International Symposium on Experimental Computational Aerothermodynamics of Internal Flows, 4-7 July 2011, Brussels, Belgium.

Computation of mixing processes related to EGR A. Sakowitz and L. Fuchs, 2011, 7th International Symposium on Turbulence and Shear Flow Phenomena, 28-31 July 2011, Ottawa, Canada.

Paper 2

Effects of velocity ratio and inflow pulsations on the flow in a T-junction using Large Eddy Simulation A. Sakowitz (AS), M. Mihaescu (MM) & L. Fuchs (LF), 2012, submitted to *Computers & Fluids*

The effects of changing the mass flow ratio between the main and the branch ratio on the secondary structures, the flow modes and the mixing quality are examined. Furthermore, pulsating inflow conditions are applied at the branch inlet mimicking EGR pulsations. The flow modes are analyzed using Dynamical Mode Decomposition (DMD). The computations and the data analysis were performed by AS under supervision of MM and guidance of LF. The paper writing was performed by AS with

help and comments of MM and LF. Parts of these results have been presented and published in:

LES of the turbulent mixing process in a T-junction with stationary and pulsating inflow conditions
A. Sakowitz and L.Fuchs, 2011, 10th International Symposium on Experimental Computational Aerothermodynamics of Internal Flows, 4-7 July 2011, Brussels, Belgium.

Computation of mixing processes related to EGR A. Sakowitz and L. Fuchs, 2011, 7th International Symposium on Turbulence and Shear Flow Phenomena, 28-31 July 2011, Ottawa, Canada.

Paper 3

Modeling of EGR Mixing in an engine intake manifold using LES A. Sakowitz (AS), S. Reifarth (SR), M. Mihaescu (MM) & L. Fuchs (LF), 2012, submitted to *Oil & Gas Science and Technology*, presented at *International Conference on LES for Internal Combustion Engine Flows, 29-30 November 2012, Paris, France.*

The flow and the EGR concentration is investigated in an intake manifold of a Scania six-cylinder Diesel engine by LES and CO_2 measurements. The results are analyzed in terms of the mixing uniformity among the cylinders and over the cylinder port cross-sections. The LES are compared to the experimental data and URANS computations. As a prerequisite for the three-dimensional computations, the boundary conditions were partly computed by one-dimensional engine simulations and experiments on the engine. The sensitivity to changes in the boundary conditions is examined by applying changes on the inlet and outlet conditions. The three-dimensional computations and the data analysis were performed by AS under supervision of MM and guidance of LF. The experiments and the one-dimensional computations were performed by SR. Except of the section *2.2 Experiments*, which was written by SR, the paper writing was performed by AS with help and comments of MM and LF.

Paper 4

Flow decomposition methods applied to the flow in an IC engine manifold A. Sakowitz (AS), M. Mihaescu (MM) & L. Fuchs (LF), 2012, submitted to *Applied Thermal Engineering*

Further details of the flow in an engine manifold, for which mixing is described in Paper 3, are given. The flow decomposition methods POD and DMD are applied to the LES data. The computations and the data analysis were performed by AS under supervision of MM and guidance of LF. The paper writing was performed by AS with help and comments of MM and LF.

Acknowledgements

This thesis would certainly not have been possible without the help and support provided by several people. I would like to thank my main supervisor, Prof. Laszlo Fuchs, for giving me the chance to do these studies and for the many enthusiastic discussions we had. My second supervisor, Dr. Mihai Mihaescu, who joined the project in January 2012, is thanked for his many suggestions and discussions, which certainly improved the quality of this thesis.

The involvement of industry into this work was appreciated very much. Dennis Konstanzer (Scania) and Christopher Håkansson (FS Dynamics & Volvo) are thanked for providing geometries, meshes and feedback. Also Vattenfall is acknowledged for providing experimental data.

Another important contribution to this work was, of course, the social environment during my time at KTH. I would like to thank all my colleagues at Mechanics for the very entertaining fika breaks, afterworks and the innebandy games.

Even though my parents were far away, they always supported me in any ways they could; for example by sending me important goods (that are missing or too expensive in Sweden) and supporting words. Thank you very much!

Last, but not least, I would like to express my love to my newly founded little family. Thank you, Hanna, for being there for me! Thank you, Kai, for doing all this funny stuff you do!

References

ANDERSSON, U., WESTIN, J. & ERIKSSON, J. 2006 Thermal mixing in a T-junction. *Tech. Rep. U 06-66, Vattenfall Research and Development AB* .

BATCHELOR, G. 1959 Small-scale variation of convected quantities like temperature in turbulent fluid, part 1. *J. Fluid Mech.* **5**, 113–133.

BATCHELOR, G., HOWELLS, I. & TOWNSEND, A. 1959 Small-scale variation of convected quantities like temperature in turbulent fluid, part 2. *J. Fluid Mech.* **5**, 134–139.

BRÜCKER, C. 1997 Study of the three-dimensional flow in a T-junction using a dual-scanning method for three-dimensional scanning-particle-image velocimetry (3-d spiv). *Exp. Therm Fluid Sci.* **14**, 35–44.

CARPINLIOGLU, M. O. & GUNDOGDU, M. Y. 2001 A critical review on pulsatile pipe flow studies directing towards future research topics. *Flow Meas. Instrum.* **12**, 163–174.

CHATTERJEE, A. 2000 An introduction to the proper orthogonal decomposition. *Current Science* **78(7)**, 808–817.

CHAUVET, T. & DIMITROVA, Z. 2008 Synergies between high EGR operation and GDi systems. *SAE Technical Paper 2008-01-0134* .

CHOI, S., PARK, W., LEE, S., MIN, K. & CHOI, H. 2011 Methods for in-cylinder EGR stratification and its effects on combustion and emission characteristics in a diesel engine. *Energy* **36**, 6948–6959.

DANCKWERTS, P. 1952 The definition and measurement of some characteristics of mixtures. *Appl. Sci. Res.* **A3**, 279–296.

DEAN, W. 1928 The stream-line motion of a fluid in a curved pipe flow. *Philos. Mag.* **5**, 673.

DEC, J. E., KELLER, J. O. & HONGO, I. 1991 Time-resolved velocities and turbulence in the oscillating flow of a pulse combustor tail pipe. *Combust. Flame* **83**, 271–292.

DIETSCH, K.-H. & KLINGEBIEL, M. 2007 *Automotive Handbook*, 7th edn. Bosch.

FERZIGER, J. H. & PERIC, M. 1996 *Computational Methods for Fluid Dynamics*. Springer.

FRANK, T., LIFANTE, C., PRASSER, H.-M. & MENTER, F. 2009 Simulation of turbulent and thermal mixing in t-junctions using URANS and scale-resolving turbulence models in ANSYS CFX. *Nuc. Eng. Des.* **240**, 2313–2328.

FRIC, T. 1995 Skewed shear layer mixing within a duct. *In: Proceedings of the 33rd Aerospace Sciences Meeting and Exhibit* **AIAA 95-0869**.

GREEN, R. M. 2000 Measuring the cylinder-to-cylinder egr distribution in the intake of a diesel engine during transient operation. *SAE Technical Paper 2000-01-2866* .

HE, S. & JACKSON, J. 2009 An experimental study of pulsating turbulent flow in a pipe. *Eur. J. Mech. B Fluids* **28**, 309–320.

HEYWOOD, J. B. 1988 *Internal Combustion Engine Fundamentals*. McGraw-Hill, New York.

HIROTA, M., ASANO, H., NAKAYAMA, H., ASANO, T. & HIRAYAMA, S. 2006 Three-dimensional structure of turbulent flow in mixing t-junction. *JSME International Journal Series B* **49**, 1070–1077.

HO, C.-M. & HUERRE, P. 1984 Perturbed shear layers. *Ann. Rev. Fluid Mech.* **16**, 365–424.

HU, L. & KAZIMI, M. 2006 LES benchmark study of high cycle temperature fluctuations caused by thermal striping in a mixing tee. *Int. J. Heat Fluid Flow* **27**, 54–64.

IGARASHI, M., M., T., KAWASHI, S. & KAMIDE, H. 2002 Experimental study on fluid mixing for evaluation of thermal striping in T-pipe junction. *Proc. of 10th Int. Conf. On Nuclear Engineering, Arlington, USA* .

KAMIDE, H., IGARASHI, M., KAWASHIMA, S., KIMURA, N. & HAYASHI, K. 2009 Study on mixing behaviour in a tee piping and numerical analyses for evaluation of thermal striping. *Nuc. Eng. Des.* **239**, 58–67.

KARTHIKEYAN, S., HARIGANESH, R., SATHYANADAN, M. & KRISHNAN, S. 2011 Computational analysis of EGR mixing inside the intake system & experimental investigation on diesel engine for LCV. *Int. J. Eng. Sci. Tech.* **3**, 2050–2058.

KOK, J. B. W. & VAN DER WAL, S. 1996 Mixing in T-junctions. *Appl. Math. Modell.* **20**, 232–243.

KOLMOGOROV, A. N. 1991 The local structure of turbulence in incompressible viscous flow for very large reynolds numbers. *Proc. R. Soc. London* **A 434**, 9–13.

KUCZAJ, A., KOMEN, E. & LOGINOV, M. 2010 Large-eddy simulation study of turbulent mixing in a T-junction. *Nuc. Eng. Des.* **240**, 2116–2122.

LAUNDER, B. & SPALDING, D. 1974 The numerical computation of turbulent flows. *Comput. Meth. Appl. Mech. Eng.* **3(2)**, 269–289.

LIANG, Y., LEE, H., LEE, K. & WU, C. 2002 Proper orthogonal decomposition and its application - part I: Theory. *J. Sound Vib.* **252(3)**, 527–544.

MAIBOOM, A., TAUZIA, X. & HETET, J.-F. 2008 Experimental study of various effects of exhaust gas recirculation (EGR) on combustion and emissions of an automotive direct injection diesel engine. *Energy* **33**, 22–34.

MAIBOOM, A., TAUZIA, X. & HETET, J.-F. 2009 Influence of EGR unequal distribution from cylinder to cylinder on NOx-PM trade off of a HSDI automotive Diesel engine. *Appl. Therm. Eng.* **29**, 2043–2050.

NAIK-NIMBALKAR, V., PATWARDHAN, A., BANJEREE, I. & PADMAKUMAR, G. VAIDYANATHAN, G. 2010 Thermal mixing in t-junctions. *Chem. Eng. Sci.* **65**, 5901–5911.

OHMI, M., IGUCHI, M. & USUI, T. 1981 Flow pattern and frictional losses in pulsating pipe flow. part 5 wall shear stress and flow pattern in a laminar flow. *Bull. JSME* **24**, 75–81.

POPE, S. 2008 *Turbulent Flows*. Cambridge University Press.

RAMANATHAN, S., HUDSON, A., STYRON, J., BALDWIN, B., IVES, D. & DUCU, D. 2011 Egr and swirl distribution analysis using coupled 1d-3d cfd simulation for a turbocharged heavy duty diesel engine. *SAE Technical Paper 2011-01-2222* .

ROWLEY, C. W., MEZIC, I., BAGHERI, S., SCHLATTER, P. & HENNINGSON, D. S. 2009 Spectral analysis of nonlinear flows. *J. Fluid Mech.* **641**, 115–127.

SCHÄFER, M. 1999 *Numerik im Maschinenbau.* Springer, Berlin.

SCHWARZ, H., DECKER, H., ROHDE, S., FELGER, G., LEMBKE, M., ZECHNALL, M., GUENTHER, D., KRAUS, B. & DIETER, W. 1988 Avgasteknik för ottomotorer - teknisk information. Bosch.

SCOTTI, A. & PIOMELLI, U. 2001 Numerical simulation of pulsating turbulent channel flow. *Phys. Fluids* **13**, 1367–1384.

SHEMER, L., WYGNANSKI, I. & KIT, E. 1985 Pulsating flow in a pipe. *J. Fluid Mech.* **153**, 312–337.

SIEWERT, R. M., KRIEGER, R. B., HUEBLER, M. S., BARUAH, P. C., KHALIGHI, B. & WESSLAU, M. 2001 Modifying an intake manifold to improve cylinder-to-cylinder EGR distribution in a DI diesel engine using combined CFD and engine experiments. *SAE Technical Paper 2001-01-3685* .

STANGLMAIER, R. H. & ROBERTS, C. E. 1999 Homogenous charge compression ignition (HCCI): Benefits, compromises, and future engine application. *SAE Technical Paper 1999-01-3682* .

TU, S. & RAMAPRIAN, B. 1983 Fully developed periodic turbulent pipe flow. part 1. main experimental results and comparison with predictions. *J. Fluid Mech.* **137**, 31–58.

WALKER, C., MANERA, A., NICENO, B., SIMIANO, M. & PRASSER, H.-M. 2010 Steady-state RANS-simulations of the mixing in a T-junction. *Nuc. Eng. Des.* **240**, 2107–2115.

WESTIN, J., T'MANNETJE, C., ALAVYOON, F., VEBER, P., ANDERSSON, L., ANDERSSON, U., ERIKSSON, J., HENRIKSSON, M. & ANDERSSON, C. 2008 High-cycle thermal fatigue in mixing tees. large-eddy simulations compared to a new validation experiment. *ICONE Proceedings* .

WILIAM, J. & DUPONT, A. 2003 Study of geometrical parameter influence on air/EGR mixing. *SAE Technical Paper 2003-01-1796* .

YOSHIZAWA, K., MORI, K., MATAYOSHI, Y. & KIMURA, S. 2003 Development of an exhaust gas recirculation distribution prediction method using three-dimensional flow analysis and its application. *J. Eng. for Gas Turbines and Power* **125**, 1066–1074.